Self-Driven Jamming in Growing Microbial Populations

Morgan Delarue, Jörn Hartung, Carl Schreck, Pawel Gniewek, Lucy Hu, Stephan Herminghaus, Oskar Hallatschek

Self-Driven Jamming in Growing Microbial Populations

Morgan Delarue[1,†], Jörn Hartung[2,†], Carl Schreck[1], Pawel Gniewek[1,3], Lucy Hu[4], Stephan Herminghaus[2] & Oskar Hallatschek[1,2]

[1]Departments of Physics and Integrative Biology, University of California Berkeley, USA. [2]Max Planck Institute for Dynamics and Self-Organization Göttingen, Germany. [3]Biophysics Graduate Group, University of California Berkeley, USA. [4]Department of Bioengineering, University of California Berkeley, USA.

† MD and JH equally contributed to this work.

In natural settings, microbes tend to grow in dense populations [1–4] where they need to push against their surroundings to accommodate space for new cells. The associated contact forces play a critical role in a variety of population-level processes, including biofilm formation [5–7], the colonization of porous media [8, 9], and the invasion of biological tissues [10–12]. Although mechanical forces have been characterized at the single cell level [13–16], it remains elusive how collective pushing forces result from the combination of single cell forces. Here, we reveal a collective mechanism of confinement, which we call self-driven jamming, that promotes the build-up of large mechanical pressures in microbial populations. Microfluidic experiments on budding yeast populations in space-limited environments show that self-driven jamming arises from the gradual formation and sudden collapse of force chains driven by microbial proliferation, extending the framework of driven granular matter [17–20]. The resulting contact pressures can become large enough to slow down cell growth, to delay the cell cycle in the G1 phase, and to strain or even destroy the microenvironment through crack propagation. Our results suggest that self-driven jamming and build-up of large mechanical pressures is a natural tendency of microbes growing in confined spaces, contributing to microbial pathogenesis and biofouling [21–26].

The simultaneous measurement of the physiology and mechanics of microbes is enabled by a microfluidic bioreactor [27–30] that we have designed to culture microbes under tightly controlled chemical and mechanical conditions. The setup, shown in Fig. 1a, is optimized for budding yeast (*S. cerevisiae*). We use this device to measure mechanical forces generated by partially-confined growing populations and the impact of those forces on both the population itself and its microenvironment.

At the beginning of each experiment, we trap a single yeast cell in the growth chamber of the device, which can hold up to about 100 cells. The cells are fed by a continuous flow of culture medium, provided by a narrow set of channels that are impassable for cells.

While cells first proliferate exponentially as in liquid culture, their growth dynamics is dramatically altered once the chamber is filled. At high density, cells move in a stop-and-go manner and increasingly push against the chamber walls. The population develops a contact pressure that increases over time until it reaches a steady state, subject to large fluctuations. Note that this contact pressure is conceptually very different from the hydrostatic pressure because water can flow in and out of cells Depending on the geometry of the outlet (Fig. 1b and c), the mean steady-state pressure can reach up to 0.7 ± 0.1 MPa. This pressure is larger than the osmotic pressure difference, ≈ 0.2 MPa (stationary phase [31]), between the interior of a budding yeast cell and the surrounding medium, and much larger than the ≈ 1 mPa needed for the cells to overcome viscous friction (Supplementary Text).

While the initial pressure build-up is similar in different devices, we find a sensitive dependence on the device geometry. The steady state pressure can be finely tuned by the shape of the outlet gate (shown in Fig. 1b and c) or the width of the outlet channel (Fig. S13).

Both the intermittent flow and pressure build-up are counterintuitive because, in all cases, the outlet channel is wide enough for cells to pass. In principle, excess cells could flow like a liquid out of the chamber. Time lapse movies (**Movie S1**) reveal that blockages in the device stabilize the cell packing and prevent flow. Cells proliferate until a sudden avalanche flushes them through the outlet (Fig. 1d and e). Another jamming event occurs, and the process repeats. These dynamics generate characteristic slow pressure increases followed by sudden pressure drops (Fig. 1c).

Jamming, intermittency and avalanches are familiar aspects of flowing sand, grains or even jelly beans [24]. To test whether the interplay of growth, collective rearrangement, and outflow of cells from the chamber can be explained by the mechanics of granular materials, we set up coarse-grained computer simulations with cells represented as elastic particles that grow exponentially and reproduce by budding. In our simulations, cells move via frictionless over-damped dynamics with repulsive contact interactions between neighbors.

Our simulations indeed reproduce the intermittent dynamics observed in the experiments (Fig. 2a–c). We find that the distribution of pressure drops have an exponential tail in both experiments and simulations (Fig. 2d) for $P > \langle P \rangle$, similar to avalanche size distributions in hopper flows [32].

Highly intermittent cell flows might reflect spatially hetero-

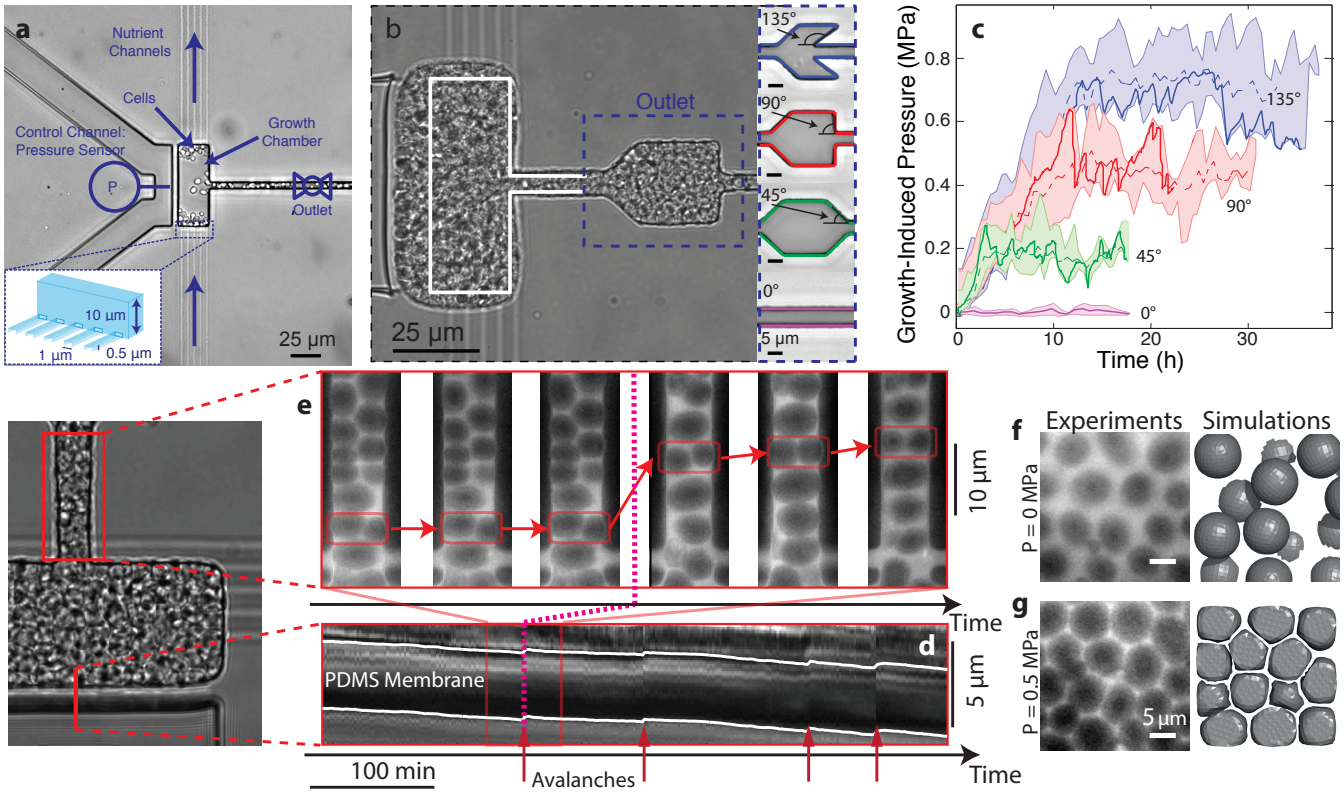

Figure 1 Self-driven jamming of microbes enables collective pressure build-up in microfluidic environments. (**a**) Budding yeast cells are grown in a growth chamber threaded by narrow nutrient channels (inset). (**b**) The jamming of excess microbes produced by proliferation in the device leads to a partial confinement of the population and a gradual build-up of a contact pressure of up to 0.65 ± 0.1 MPa (in the shown experiment), which strongly deforms the device (white line represents the undeformed layout). The steady-state pressure generated in a given device depends on the geometry of the outlets (**b**, right), which effectively act as leaky one-way valves. The resulting time-dependent pressure curves are shown in (**c**) for different outlets. The pressure measurements were enabled by an automatic feedback system that actively controls the deformation of a thin membrane separating the growth chamber and a control channel (see **a** and Supplementary Text). The bold curves correspond to one realization of the experiment, which is characterized by large pressure fluctuations due to gradual jamming and sudden unjamming. The shaded region represents the envelope of the replicates: all replicates are binned together, and within each bin, the minimum and the maximum define the shading. The dashed line corresponds to the mean of all realizations. The cellular flows exhibits collective features known from physics of jamming in granular media: The outflow of cells is not steady but consists of periods of stasis, accompanied by pressure-build up, and sudden cell avalanches and pressure drops. This can be seen in time lapse movies (**Movie S1**) as well as Kimographs: (**d**) shows the random zig-zag motion of the chamber membrane and (**e**) shows the flow through the outlet before, during and after an avalanche with one snapshot every 20 minutes. Note that, depending on the local stresses, cells assume shapes from nearly spherical (**f**, low stress) to nearly polyhedral (**g**, high stress). (**f, g**, left) Micrographs taken close to the coverslip at the bottom of the chamber. (**f, g**, right) Mass-spring simulations, in which cell walls are represented as (at vanishing contact pressure) spherical meshworks of springs (Supplementary Text). For better visualization, the simulations only show the first layer of cells. The depths of this layer are 5.25 μm and 1.7 μm for low and high pressure respectively.

geneous mechanical stresses, a hallmark of driven granular materials [17–20]. Assuming that cell shape deformation is indicative of the forces between cells, we developed a non-invasive method to infer these forces (Fig. 2f, supplementary text, and Fig. S1). Using this approach, we analyzed microscopy images to determine stress distributions of crowded populations. Both *S. cerevisiae* experiments and our coarse-grained simulations exhibit disordered cell packings that are stabilized by heterogeneous force networks (Fig. 2f and g). Stress is highly localized along branching "force chains" [17, 18] while adjacent "spectator cells" [33] experience very little mechanical stress.

We find that jamming-induced contact forces can become so large that they feed back on the cell physiology. Indeed, a feedback on both cell shape and the dynamics of cell growth is evident in experiments where we place two devices of different steady state pressures next to one another, as seen in the time lapse movie (**Movie S2**). These devices only differ by the width of their outlet channels (5μm vs. 7.5μm). We find that an increased outlet channel width leads to an increased mean avalanche size, and correspondingly, a smaller mean pressure (Fig. S13). To quantify the feedback on growth, we estimate the net growth rate, which is the difference between birth and death rate, in our microfluidic bioreactors by measuring mean cell outflow rate at steady state (supplementary text). We find that the growth rate decays roughly exponentially with pressure until growth is undetectable at a stalling pressure of about 1 MPa (Fig. 3c). The stalling pressure, or homeostatic pressure [34], is obtained by using a special device with a "self-closing valve", in which yeast populations fully confine themselves by the pressure they build up, as seen in Fig. 3a. In this device, the rate of pressure increase gradually decays with pressure until saturation (Fig. 3b). This diminishing return is due to smaller growth rates at higher pressures, and serves as another, dynamical measure for the feedback between contact pressure and growth rate.

Control experiments supported by finite element simulations show that cells are well-fed and viable even at the highest densities suggesting a mechanobiological origin for the reduced growth rates (Supplementary Text and Figs. S3 and S4).

As a first step to uncover the mechanistic basis for the force-growth feedback, we have explored the impact of contact forces on the pace of cell cycle progression. In budding yeasts, the late G1 checkpoint Start, homolog to the mammalian Restriction point, controls the irreversible cell commitment to division [35]. Passing of the checkpoint requires multiple phosphorylations of the repressor Whi5, upon which Whi5 is exported out of the nucleus until the cell cycle is completed. As a consequence, Whi5 is localized in the nucleus in the G1 phase prior to Start, and cytosolic otherwise (Fig. 3d, top). Using a mutant that express fluorescently labeled Whi5 thus enabled us to probe the cellular commitment to cell division. We found that an increased contact pressure is accompanied by an increase in the fraction of cells with nuclear Whi5 signal (Fig. 3d), suggesting a force-induced slowdown of the cell cycle in G1. This finding is consistent with the view of the late G1 checkpoint as an integrator of numerous stresses, including osmotic, chemical and heat shock stresses [36–38]. Force-induced cell cycle arrest has been observed in mammalian cells [39, 40], but the associated mechanical stresses are two to three orders lower than the stalling pressure measured in our experiments.

Perhaps the most salient consequence of growth-induced pressure is cell shape deformations. While budding yeast cells grown in the absence of mechanical stresses are nearly spherical, we observe that they tend to morph into convex polyhedra as the population pressure becomes growth-limiting (Fig. 1f and g). Close to the stalling pressure, the packing resembles the structure of a dry foam [41], consisting of cells with nearly flat faces and sharp edges in between, shown in Fig. 2f. The pressure-induced cell shape deformation can be best visualized at the interface between coverslip and cell population: the cell-coverslip contact area increases as the growth-induced pressure increases (Fig. S6). Our simulations further suggest that, in our experiments, the osmotic pressure inside the cells may increase as a function of the growth-induced pressure (Fig. S6).

Most microbial cells are sticky [42, 43]. Indeed, while our lab strains of budding yeast have been domesticated to become non-sticky, wild strains can have strong, velcro-like intercellular fiber connections [44]. We find that while sticky yeasts develop in our microfluidic devices a very similar maximal pressure as the lab strains do (Fig. 3b), they develop substantial contact pressures under much weaker confinement (Fig. 4a). Our coarse-grained simulations likewise suggest that attractive interactions promote jamming: The measured build up of pressure is much larger than expected under a non-granular model of a liquid droplet with surface tension, in which jamming is impossible (Fig. 4c and d).

Bacteria and fungi have the ability to colonize a wide range of porous media, including tiny cavities barely larger than their cell size [3, 4]. Our work suggests that self-driven jamming of growing microbes can emerge in these microenvironments as it does in our microfluidic devices if chemical resources are sufficiently abundant.

The resulting growth-induced forces endow biofilms with the potential to remodel, or even destroy, their micro-environment. This could aid microbes in penetrating the soft tissues of host organisms [10–12], or to invade soil, where most microbes grow in pores of several micro-meter in diameters [3, 4]. At this length scale, it is possible that the growth-induced pressures measured here contribute to straining of even stiff materials. Indeed, when we grow budding yeast populations inside agar gels, we observe the formation and propagation of cracks (Fig. 4d, Fig. S8 and time lapse movie **Movie S5**). Thus, just

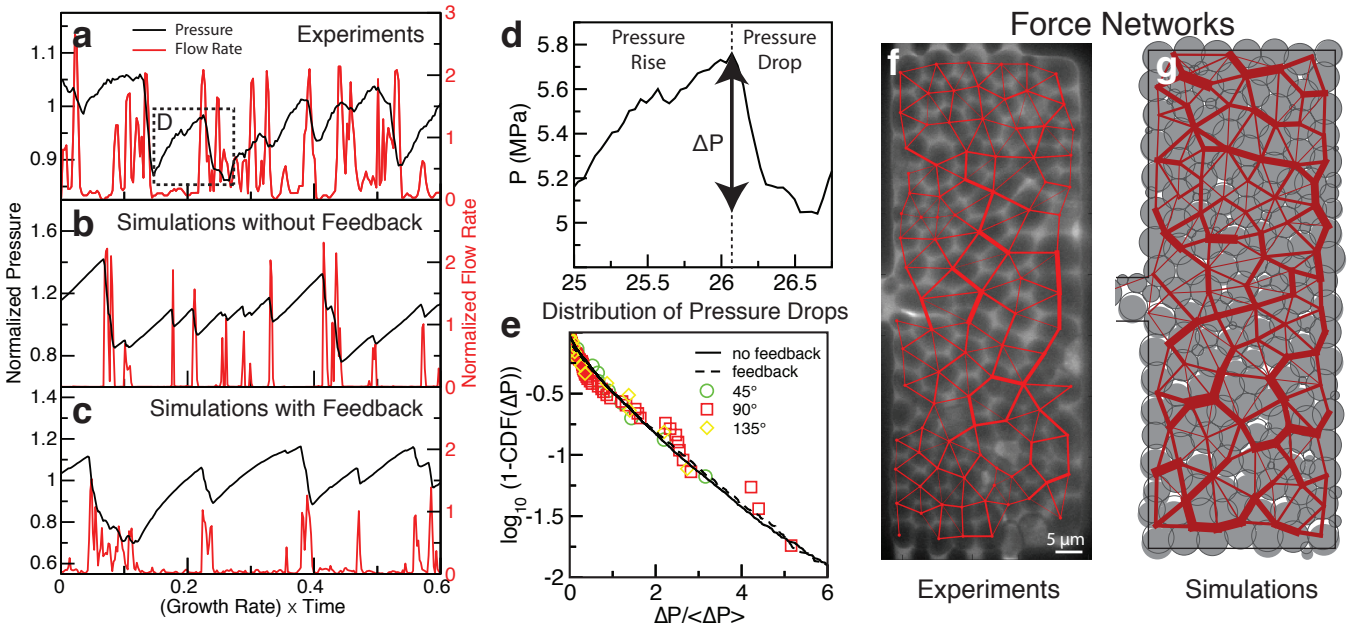

Figure 2 Pressure fluctuations and intermittent flows of partially confined budding yeast populations can be reproduced in simulations of proliferating elastic particles. (**a**) Experimental pressure time series are characterized by periods of gradual pressure build-up and sudden pressure drops. (**b**) Simulations show that such time series are the generic outcome of jammed elastic particles proliferating in confined spaces. (**c**) A feedback of pressure onto growth, reported in Fig. 3c below, further improves our simulations. The gradual pressure increases prior to avalanche events show diminishing return similar to the experimental time series in (**a**). Pressure drops during avalanche events, defined as the pressure change from the peak pressure prior to an outflow event to the base pressure just after the event (**d**), are nearly exponentially distributed for drops larger than the mean pressure drop, $\langle \Delta P \rangle$, in both experiments (**e**: symbols) and coarse-grained simulations (**e**: lines). We can estimate inter-cell contact forces in our experiments by measuring the area of contact between two cells through image analysis. (**f**) The resulting network of contact forces in packings of budding yeast cells shows a heterogeneous distribution of mechanical stresses (pressure on the membrane: 0.5 MPa). (**g**) Force networks obtained from simulations of exponentially growing budding cells. In both (**f**) and (**g**), large forces are clustered into chain-like structures. A movie illustrating the dynamics of force networks in our experiments can be seen **Movie S3**, and a coarse-grained simulation movie can be seen **Movie S4**. For our simulations, we used box and outlet sizes that match the microfludic chamber and parameterized the over-damped dynamics using the experimental flow rate and pressure fluctuation data (Supplementary Text).

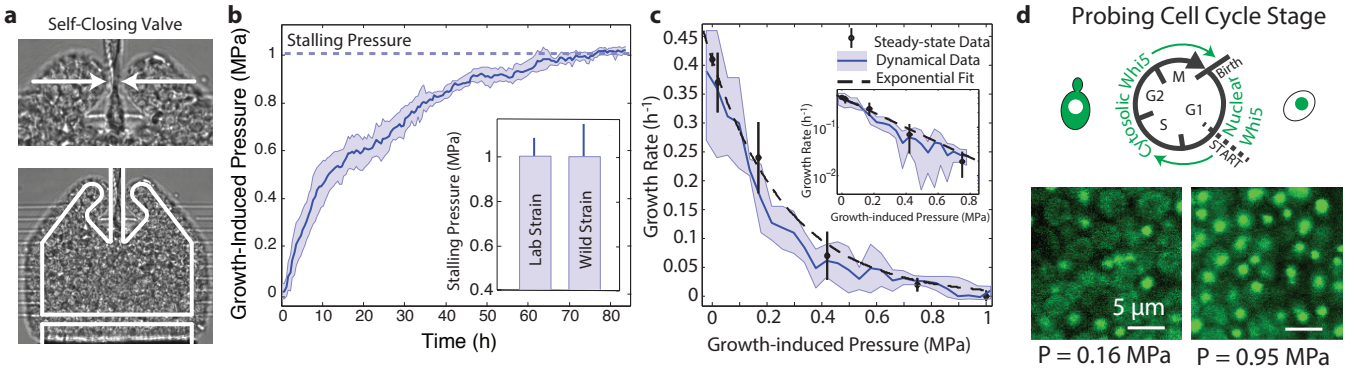

Figure 3 Pressure-induced slow down of growth. (**a**) Budding yeast populations can be fully confined using a "self-closing" device that takes advantage of the contact pressure developed by the population to close the inlet/outlet channel. The cells are fed through narrow nutrient channels, as in 1**a**. The layout of the undeformed device is shown in white. (**b**) The time-dependent pressure curve in the self-closing devices shows a diminishing return: The rate of increase of the growth-induced pressure in the fully confined region gradually slows until it stops at the stalling pressure of 1 ± 0.1 MPa (5 replicates, mean $\pm$ standard deviation). Inset: stalling pressure measured for the lab strain and the wild strain. (**c**) Growth rate as a function of growth-induced pressure, estimated in two ways (supplementary text): The black points represent net growth rates determined from the cell flow out of our leaky devices in the steady-state (black points; ≥ 5 replicates, mean $\pm$ standard deviation). The continuous blue line, on the other hand, has been inferred from the diminishing return in the dynamical data of (**b**) under a quasi-steady state assumption (supplementary text; shading indicates $\pm$ standard deviation). The dashed curves represents an exponential fit to the steady-state data (k = 0.41 (h^{-1}) exp(-P/0.28 (MPa))). (**d**) We probed the cell cycle progression using mutants that express fluorescently labeled Whi5 repressor proteins. In the G1 phase of the cell cycle prior to the checkpoint Start, Whi5 is localized in the nucleus yielding a subcellular fluorescent focus (see scheme). We find that at high contact pressures of 0.95 MPa almost four times as many cells exhibiting a nuclear Whi5 signal than at low pressures of P = 0.16 MPa (Fig. S5).

like jamming of granular media can threaten the mechanical integrity of their confinements, which can lead to the bursting of grain silos [32, 45], it could also be an important mechanical aspect of host invasion [10–12] and biofouling [21].

We argue that the mechanism underlying self-driven jamming, cell proliferation, extends the notion of driven granular materials, which are usually jammed by external forces, such as shear, compression, or gravity [17–20]. On a fundamental level, cell proliferation and death are unique driving forces because they alter the number of macroscopic degrees of freedom, and thus directly affect Maxwellian rigidity criteria for jammed materials [46, 47]. New granular physics may also result from biological features that have no analog in traditionally-driven granular materials. For instance, the pressure-growth feedback, that we have described above, could homogenize force networks and enhance pressure buildup, as our simulations indicate (Fig. S11). Intermittent flows may be influenced by the shape of cells, as rod-like cells tend to align spontaneously, thus increasing the packing fraction [48] (Fig. S12). We also expect cell motility [49] and viscoelastic extracellular substances [6], expressed by many microbes to promote biofilm formation, to engage in a rich mechanical interplay with the packing of growing cells in confined spaces.

Acknowledgments

We would like to thank Jasper Rine, Jeremy Thorner and Liam Holt for helpful discussions, and Nils Podwitz and Hedvika Toncrova for their contributions at the initial stages of the project. Research reported in this publication was supported by the National Institute Of General Medical Sciences of the National Institutes of Health under Award Number R01GM115851, by a Simons Investigator award from the Simons Foundation (O.H.) and by the German Research Foundation (DFG) in the framework of the SFB 937/A15. The content is solely the responsibility of the authors and does not necessarily represent the official views of the National Institutes of Health.

Author Contributions

O.H. designed and supervised the study. M.D., J.H., S.H. and O.H. designed the microfluidic experiments, M.D. and J.H. developed the software and performed experiments. M.D., J.H., and L.H. fabricated devices. M.D. and L.H. performed Comsol simulations, P.G. implemented and performed the mass-spring simulations, and C.S. implemented and performed the coarse-grained simulations. M.D., J.H., C.S., P.G. and O.H. interpreted the data and wrote the manuscript.

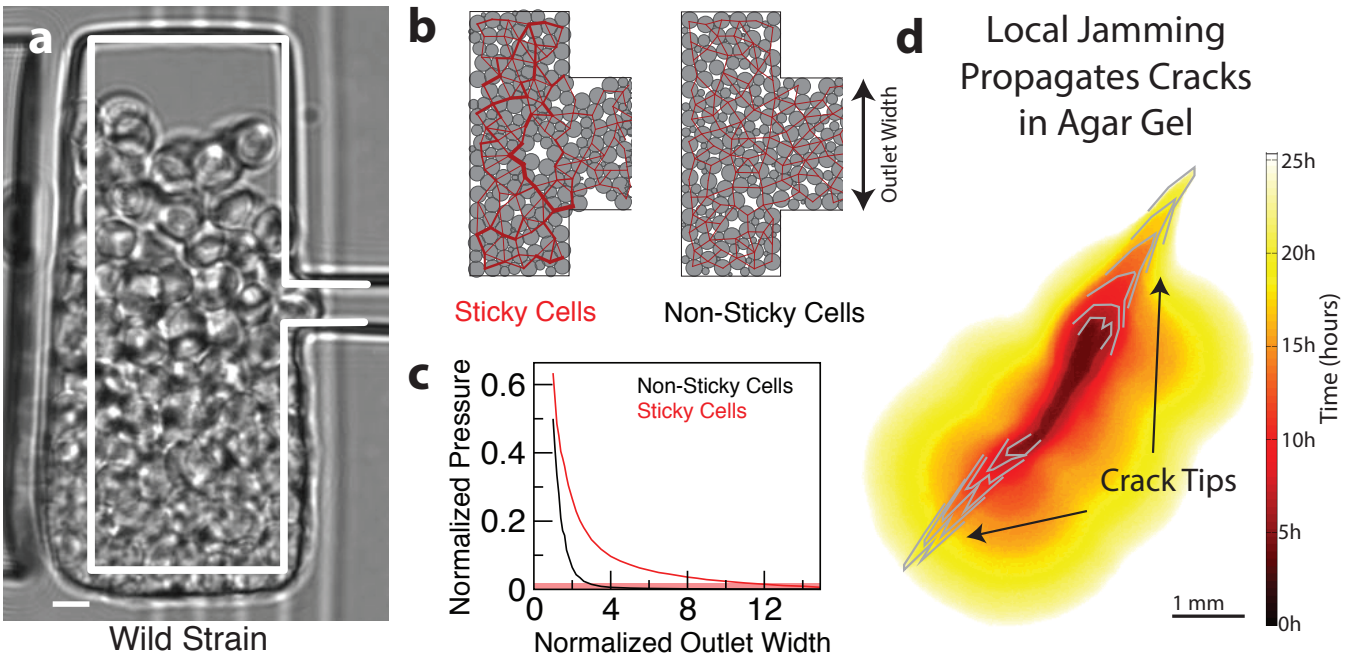

Figure 4 Self-driven jamming is promoted by stickiness and can remodel the microenvironment. (**a**) Wild strains of yeast stick together via strong velcro-like connections between cells [44]. This stabilizes the spherical growth of the population against shear stresses. (**b, c**) Simulations show that even weak attractive forces between cells can strongly promote jamming. (**b**) Packing of slightly sticky cells (right, supplementary text) exhibit a force network with pronounced force chains in contrast to the non-sticky case for the shown device. (**c**) The increase in growth-induced pressure (steady-state) with stickiness is much larger than expected from the continuum limit (red base line) over a broad range of outlet sizes (supplementary text). (**d**) Gradual propagation of agar gel cracks by growing populations of budding yeast (lab strain). Cells grow out of a pre-existing agar crack and, at the same time, propagate the crack tips inside the agar. A time-lapse movie of the crack propagation is available **Movie S5**.

References

[1] Watnick, P. and Kolter, R. Biofilm, city of microbes. *Journal of bacteriology* **182**, 2675–2679 (2000).

[2] Fanning, S. and Mitchell, A.P. Fungal biofilms. *PLoS Pathog* **8**, e1002585 (2012).

[3] Torsvik, V. and Øvreås, L. Microbial diversity and function in soil: from genes to ecosystems. *Current Opinion in microbiology* **5**, 240–245 (2002).

[4] Ranjard, L. and Richaume, A. Quantitative and qualitatice microscale distribution of bacteria in soil. *Research in Microbiology* **152**, 707–716 (2001).

[5] Wilking, J.N. *et al*. Liquid transport facilitated by channels in *Bacillus subtilis* biofilms. *Proceedings of the National Academy of Sciences* **110**, 848–852 (2013).

[6] Wilking, J.N., Angelini, T.E., Seminara, A., Brenner, M.P. and Weitz, D.A. Biofilms as complex fluids. *MRS Bulletin* **36**, 385–391 (2011).

[7] Asally, M. *et al*. Localized cell death focuses mechanical forces during 3d patterning in a biofilm. *Proceedings of the National Academy of Sciences* **109**, 18891–18896 (2012).

[8] Cunningham, A.B., Characklis, W.G., Abedeen, F. and Crawford, D. Influence of biofilm accumulation on porous media hydrodynamics. *Environmental Science and Technology* **25**, 1305–1311 (1991).

[9] Rittman, B.E. The significance of biofilms in porous media. *Water Resources Research* **29**, 2195–2202 (1993).

[10] Gow, N.A.R., Brown, A.J.P. and Odds, F.C. Fungal morphogenesis and host invasion. *Current opinion in microbiology* **5**, 366–371 (2002).

[11] Money, N.P. Turgor pressure and the mechanics of fungal penetration. *Canadian journal of botany* **73**, 96–102 (2002).

[12] Foster, T.J., Geoghegan, J.A., Ganesh, V.K. and Höök M. Adhesion, invasion and evasion: the many functions of the surface proteins of *Staphylococcus aureus*. *Nature Reviews Microbiology* **12**, 49–62 (2014).

[13] Smith, A.E., Zhang, Z., Thomas, C.R., Moxham, K.E. and Middelberg A.P.J. The mechanical properties of *Saccharomyces cerevisiae*. *Proceedings of the National Academy of Science* **97**, 9871–9874 (2000).

[14] Minc, N., Boudaoud, A. and Chang, F. Mechanical forces of fission yeast growth. *Current Biology* **19**, 1096–1101 (2009).

[15] Stenson, J.D., Thomas, C.R. and Hartley, P. Modelling the mechanical properties of yeast cells. *Chemical Engineering Science* **64**, 1892–1903 (2009).

[16] Tuson, H.H. *et al*. Measuring the stiffness of bacterial cells from growth rates in hydrogel of tunable elasticity. *Molecular micrbiology* **84**, 874–891 (2012).

[17] Radjai, F., Jean, M, Moreau, J.J. and Roux, S. Force distribution in dense two-dimensional granular systems. *Physical Review Letter* **77**, 274 (1996).

[18] Majmudar, T.S. and Behringer R.P. Contact force measurement and stress-induced anisotropy in granular materials. *Nature* **435**, 1079–1082 (2005).

[19] Bi, D, Zhang, J, Chakraborty, B. and Behringer, R.P. Jamming by shear. *Nature* **480**, 335-358 (2011).

[20] Heussinger, C. and Barrat, J.L. Jamming transition as probed by quasistatic shear flow. *Physical Review Letter* **102**, 218303 (2009).

[21] Warscheid, T.H. and Braams J. Biodeterioration of stone: a review. *International biodeterioration and biodegradation* **46**, 343–368 (2000).

[22] Seebacher, C. *et al*. Onychomycosis. *Mycosis* **50**, 321–327 (2007).

[23] Douglas, L.J. Candida biofims and their role in infection. *Trends in microbiology* **11**, 30–36 (2003).

[24] GDR MiDi. On dense granular flows. *The european Physical Journal E* **14**, 341–365 (2004).

[25] Hall-Stoodley, L., Costerton, J.W. and Stoodley, P. Bacterial biofilms: from the natural environment to infectious diseases. *Nature Reviews Microbiology* **2**, 95–108 (2004).

[26] Park, JA. *et al*. Unjamming and cell shape in the asthmatic airway epithelium. *Nature Materials* **14**, 1040–1048 (2015).

[27] Rowat, A., Bird, J., Agresti, J., Rando, O. and Weitz, D. Tracking lineages of single cells in lines using a microfluidic device. *Proceedings of the National Academy of Sciences* **106**, 18149–18154 (2009).

[28] Cho, H. *et al*. Self-organization in high-density bacterial colonies: efficient crowd control. *PLoS Biology* **5**, e302 (2007).

[29] Balagaddé F.K., You, L., Hansen, C.L., Arnold, F.H. and Quake, S.R. Long-term monitoring of bacteria undergoing programmed population control in a microchemostat. *Science* **309**, 137–140 (2005).

[30] Charvin, G. Cross, F.R. and Siggia, E.D. A microfluidic device for temporally controlled gene expresion and long-term fluorescent imaging in unperturbed dividing yeast cells. *PLoS One* **3**, e1468–e1468 (2008).

[31] Martinez de Maranon, I., Maréchal, P.A. and Gervais, P. Passive response of *Saccharomyces cerevisiae* to osmotic shift: cell volume variations depending on the physiological state. *Biochemical and biophysical research communications* **227**, 519–523 (1996).

[32] Zuriguel, I., Garcimartin, A., Maza, D., Pugnaloni, L.A. and Pastor, J.M. Jamming during the discharge of granular matter from a silo. *Physical Review Letter* **81**, 1841 (1998).

[33] Cates, M.E., Wittmer, J.P., Bouchaud, J.P. and Claudin, P. Jamming, force chains, and fragile matter. *Physical Review Letter* **81**, 1841 (1998).

[34] Basan, M., Risler, T., Joanny, J.F., Sastre-Garau, X. and Prost, J. Homeostatic competition drives tumor growth and metastatic nucleation. *HFSP Journal* **3**, 265–272 (2009).

[35] Charvin, G., Oikonomou, C., Siggia, E.D. and Cross, F.R. Origin of irreversibility of cell cycle start in budding yeast. *PLoS Biology* **8**, e1000284 (2010).

[36] Escoté, X., Zapater, M., Clotet, J. and Posas, F. Hog1 mediates cell-cycle arrest in G1 phase by dual targeting of Sic1. *Nature Cell Biology* **6**, 997–1002 (2004).

[37] Shapiro, G.I. and Harper, J.W. Anticancer drug tragets: cell cycle and checkpoint control. *The journal of clinical investigation* **104**, 1645–1653 (1999).

[38] Rowley, A., Johnston, G.C., Butler, B, Werner-Washburne, M and Singer, R.A. Heat shock-mediated cell cycle blockage and G1 cyclin expression in the yeast *Saccharomyces cerevisiae*. *Molecular and cellular biology* **13**, 1034–1041 (1993).

[39] Huang, S., Chen, C.S. and Ingber, D.E. Control of cyclin D1, p27Kip1, and cell cycle progression in human capillary endothelial cells by cell shape and cytoskeletal tension. *Molecular biology of the cell* **9**, 3179–3193 (1998).

[40] Delarue, M. *et al*. Compressive stress inhibits proliferation in tumor spheroids through a volume limitation. *Biophysical Journal* **107**, 1821–1828 (2014).

[41] Weaire, D. and Fortes, M.A. Stress and strain in liquid and solid foam. *Advances in Physics* **43**, 685–738 (1994).

[42] Dufrêne Y.F. Sticky microbes: forces in microbial cell adhesion. *Trends in microbiology* **6**, 376–382 (2015).

[43] Soll, D.R. Candida bioilms: is adhesion sexy? *Current Biology* **18**, R717–R720 (2008).

[44] Váchová, L. *et al*. Flo11p, drug efflux pumps, and the extracellular matrix cooperate to form biofilm yeast colonies. *The journal of cell biology* **194**, 679–687 (2011).

[45] Dogangun, A., Karaca, Z., Durmus, A. and Sezen, H. Cause of damage and failures in silo structures. *Journal of performance of constructed facilities* **23**, 65–71 (2009).

[46] Maxwell, J.C. On the calculation of the equilibrium and stiffness of frames. *Philos. Mag.* **27**, 294–299 (1864).

[47] Wyart, M., Silbert, L.E., Nagel, S.R. and Witten, T.A. Effect of compression on the vibrational modes of marginally jammed solids. *Physical Review E* **72**, 051306 (2005).

[48] Volfson, D., Cookson, S., Hasty, J. and Tsimring, L.S. Biomechanical ordering of dense cell populations. *Proceedings of the National Academy of Sciences* **105**, 15346–15351 (2008).

[49] Bi, D., Yang, X., Marchetti, M.C., Manning, L.M. Motility-driven glass and jamming transitions in biological tissues. *arXiv preprint arXiv:1509.06578* (2015)

Self-Driven Jamming in Growing Microbial Populations

Supplementary Information

Morgan Delarue[1,†], Jörn Hartung[2,†], Carl Schreck[1], Pawel Gniewek[1,3], Lucy Hu[4], Stephan Herminghaus[2], and Oskar Hallatschek[1]

[1]*Departments of Physics and Integrative Biology, University of California, Berkeley, CA 94720*
[2]*Biophysics and Evolutionary Dynamics Group, Max Planck Institute for Dynamics and Self-Organization, 37077 Göttingen, Germany*
[3]*Biophysics Graduate Group, University of California Berkeley, USA.*
[4]*Department of Bioengineering, University of California Berkeley, USA.*
[†]*MD and JH equally contributed to this work*

Supplementary Methods

Yeast strains and growth conditions: *S. cerevisiae* cells (S288C background, with a Whi5-GFP construct, courtesy of J. Thorner, UC Berkeley, USA) and wild undomesticated cells (BR-103F strain, courtesy of Palkova lab at Charles University in Czech Republic) are cultured in complete synthetic medium (CSM, 20 g/L glucose) at 30^o C. The device is loaded with cells in exponential phase.

Preparation of the micro-fluidic bioreactor ("Mechano-chemostat"): The mold consists of 2 layers of different heights, each layer prepared using a classical soft lithography protocol described in Ref. [1]. The first layer is prepared using SU 2000.5 negative photoresist (0.5 μm height), and the second using SU 2010 (10 μm height). Polydimethylsiloxane (PDMS, Sylgard 184, Dow Corning, USA) is mixed with the curing agent (ratio 1:10 in mass), poured onto the mold, and cured overnight at 60^o C. PDMS is bound to no1 thickness glass slides through an oxygen plasma generated by a reactive ion etcher (RIE) machine (P_{02} = 200 mTorr, exposure time = 20 sec). Prior to loading the device, the surface is treated with Pluronics 127 (VWR, USA) as in Ref. [2] to decrease any non-specific adhesion that could result in cell-PDMS adhesion or friction.

Two methods for measuring the growth-induced pressure: To measure the contact pressure generated by the population, we monitor the position of a 4μm thick membrane separating the growth chamber and a control channel. We adjust the hydrostatic pressure every 30 seconds to keep the membrane at a fixed position. In this way, we ensure that the known hydrostatic pressure mirrors the mechanical contact pressure with a precision of 0.02 MPa.
Finite element simulations (Comsol) show that, in the absence of a hydrostatic control pressure, the deformation of the membrane is proportional to the contact pressure in the growth chamber. This linear relation can be used to convert the deformation of the membrane into the growth-induced pressure, with a precision of 0.05 MPa. However, this second method of measuring a growth-induced pressure first requires a calibration of the Young's modulus of the PDMS device. When necessary, the calibration is done before each experiment. On average, we measure a PDMS Young's modulus of 2 MPa.

Visualizing cell deformations and the contact area between cells and the coverslip: FITC-conjugated Dextran (3kDa, Invitrogen) is added to the culture medium, at a concentration of 0.1 mg/mL. Since Dextran is not internalized by single yeast cells [3], it stains the extracellular space, and enables the imaging of cell deformation. The contact between cells and the coverslip is imaged by reflectometry. Briefly, we shine a 635 nm

laser on the sample through a pinhole closed to a minimum, to obtain an optical slice of 0.3 μm. The reflected light is collected without filter, so that local changes in refractive index can be measured at the level of the glass slide. Typical images of cell deformations are shown in the main Letter (Fig. 1), and images obtained by reflectometry are shown in Fig. S6a.

Dependence of contact surface area on pressure: We measure the cell contact area at the interface between the coverslip and cell population, and compare it to our Mass-Spring simulations (see below). Reflectometry reveals that the average fraction of the coverslip that is in contact with cells increases as the population pressure increases, shown in Fig. S6a. We find that the experimentally measured growth-induced pressure increases super-linearly with surface coverage, contradicting our pressurized-shell null model. This may indicate that the yeast cell turgor pressure increases with growth-induced pressure (Fig. S6b).

Measuring the steady-state and instantaneous growth rate: Each outlet design, shown in Fig. 1b (right), leads to a different steady-state pressure, and a different steady-state cell outflow rate. We measure the cell outflow rate J_{cell} from time lapse movies using a custom-made particle image velocimetry algorithm (Matlab), and infer the growth rate in the chamber as $k = J_{\text{cell}}/\text{V}_{\text{ch}}$, where V_{ch} is the volume of the growth chamber.
Alternatively, we can estimate the instantaneous growth rate from the pressure vs. time relationship measured for the self-closing device. Since the cells are fully trapped in the growth chamber, the time-derivative of the pressure is directly proportional to the growth rate. The proportionality depends on the packing fraction of the cells (ϕ) and on the volume of the chamber (V).
We infer the instantaneous growth rate γ of the cells by

$$\gamma = \frac{\partial_t V_c}{V_c}$$

where V_c is the volume occupied by the cells. By definition, the packing fraction is the fraction of volume occupied by cells divided by the volume of the chamber:

$$\phi = \frac{V_c}{V}$$

Hence,

$$\gamma = \partial_t \log\phi + \partial_t \log V$$

Now we assume that, at any time, the packing fraction and the chamber volume only depend on the pressure: $V(t) = V(P(t))$ and $\phi(t) = \phi(P(t))$. This quasi-steady state assumption is acceptable only if the cells can adapt their growth rates sufficiently fast to the current pressure curve or, conversely, that the pressure changes sufficiently slowly.
This enables us to rewrite the growth rate:

$$\gamma = \partial_t P\,(\partial_P \log\phi + \partial_P \log V)$$

In order to plot the growth rate γ as a function of growth-induced pressure, we need three pieces of information: the time-derivative of the pressure, the packing fraction, and the pressure-dependency of the volume of the growth chamber. The packing fraction is measured using exclusion fluorescence technique (see Fig. S2a and S2c), and the dependency on pressure of the volume of the chamber is calculated through finite element simulations (Comsol) (Fig. S2b).
As shown in Fig. S2d, the growth-rate vs pressure relationship obtained in this way is in good agreement with the more direct steady-state measurements. This justifies our steady-state assumptions and suggests that the feedback on growth should act as fast or faster than the typical division time.

Inferring force maps: The interface area between cells in contact is used to estimate the contact force between the cells. To this end, we have modeled the mechanical response of budding yeast cells in the simplest possible way by assuming that a cell responds to contact forces like a pressurized elastic shell, as illustrated in Fig. 2f. The force between cells in contact is then given by $F = PA \propto Pl^2$, where A is the area of contact, P is the cell turgor pressure, and l is the projection of the contact surface onto the measurement plane. This takes into account the effects of turgor pressure and the near-inextensibility of the cell wall, but assumes that these effects dominate over elastic energies due to bending of the cell wall or cytoskeleton (the turgor pressure of ≈ 0.2 MPa [4] is nearly two orders of magnitude larger than the elastic moduli of cytoskeletal networks). Single-cell studies [5, 6, 7, 8] have indeed found that compressed *S. cerevisiae* cells exert forces proportional to the area of contact, in agreement with a model that incorporates only internal pressure and cell wall stretching even for large deformations. We further validate our approach by performing simulations of deformable cells composed of spring networks, which show similar deformations as *S. cerevisiae* cells at corresponding pressures. The simulations are described in the next paragraph and in Fig. S1 and Fig. S7.

Description of Mass-Spring simulation: The mechanics of a budding yeast cell is primarily controlled by the mechanics of the cell wall and the turgor pressure [8]. In our "mass-spring" (MS) simulations, the cell wall is represented as a spherical meshwork of springs, obtained from surface triangulation, and connecting set of vertices. The neighbor vertices, separated by a vector $\mathbf{R}$, are held together via Hookean spring interactions:

$$\mathbf{F}(\mathbf{R}) = k_{\mathrm{MS}}\mathbf{R}(1 - R_0/R) \tag{1}$$

where k_{MS} is a spring constant, and R_0 is a length of the relaxed spring. The Hookean spring constants are taken to be the same and related to the Young's modulus by the following equation:

$$k_{\mathrm{MS}} = \frac{2Et}{1-\nu} \cdot \frac{A_0}{\sum_i L_i^2} \tag{2}$$

where E is Young's modulus, ν is cell wall Poisson's ratio, t is the cell wall thickness, A_0 is the initial cell surface area, and L_i is the relaxed length of the i^{th} spring [9].
The overlap between two non-bonded vertices is modeled by Hertzian repulsive force:

$$\mathbf{F}(\mathbf{R}) = -\frac{4}{3}h^{3/2}E^*\sqrt{R^*}\hat{\mathbf{R}} \tag{3}$$

where $E^* = E/2(1-\nu^2)$ is an effective Young's modulus, E is cell wall Young's modulus, ν is cell wall Poisson's ratios, $R^* = 0.5 \cdot R_{\mathrm{vert}}$ is an effective radius, R_{vert} is a radius of a vertex, here set to be the same as the cell wall thickness t, $h = 2 \cdot R_{\mathrm{vert}} - R$ is an overlap between two vertices, and $\hat{\mathbf{R}}$ is a unit vector along $\mathbf{R}$.
The overlap between a vertex and box walls is modeled similarly but with an effective radius $R^* = R$, and an effective Young's modulus:

$$\frac{1}{E^*} = \frac{1-\nu_{\mathrm{vert}}^2}{E_{\mathrm{vert}}} + \frac{1-\nu_{\mathrm{box}}^2}{E_{\mathrm{box}}} \tag{4}$$

The force due to the cell volume-dependent turgor pressure $\Pi(V_{\mathrm{cell}})$ on vertex i is calculated as:

$$F_\Pi(\mathbf{r}_i) = \nabla_{\mathbf{r}_i}\left(\Pi(V_{\mathrm{cell}})V_{\mathrm{cell}}\right) \tag{5}$$

where $V_{\mathrm{cell}}(\mathbf{r}_1, ..., \mathbf{r}_{N_{\mathrm{vert}}})$ is a function of the N_{vert} vertices triangulating the cell surface and the volume change for the vertex i is calculated using tetrahedral volume defined by the vertex i, its neighboring vertices in the meshwork, and center of the mass. The equations of motion of over-damped dynamics have been solved using

Heun's method (explicit second-order Runge-Kutta method). In the simulations for all vertices (box wall) Young's modulus E_{vert} = 150 MPa (E_{box} = 200 MPa) and Poisson's ratio $\nu_{vert} = \nu_{box} = 1/2$ are set the same, turgor pressure is $\Pi = 1.0$ MPa (unless stated otherwise), cell wall thickness is $t = 0.1\mu$m, and the initial cell radius is $R_0 = 2.5\mu m$.

Coarse-grained simulations of proliferating elastic particles: In our 2D coarse-grained simulations, illustrated in Fig. S9, cells are modeled as two frictionless rigidly-attached spherical lobes [10] (mother and bud) that grow exponentially at rate γ_i by bud expansion (Eq. 1), move according to over-damped dynamics with mobility μ (Eqs. 2 and 3), and interact via repulsive spring forces with elastic modulus k (Eq. 4)

$$\begin{aligned} \dot{a}_i &= \gamma_i a_i && (6)\\ \dot{\mathbf{r}}_i &= \mu \mathbf{F_i} && (7)\\ \dot{\theta}_i &= \frac{m}{I}\mu T_i && (8)\\ V &= \sum_{ikjl} \frac{1}{2} k_{\mathrm{CG}} \delta_{ik,jl}^2 \Theta(\delta_{ik,jl}) && (9) \end{aligned}$$

where $a_i = \frac{\pi}{4}(\sigma_{i,\mathrm{mother}}^2 + \sigma_{i,\mathrm{bud}}^2)$ is the cell area, $\sigma_{i,\mathrm{mother}}$ ($\sigma_{i,\mathrm{bud}}$) is the diameter of the mother (bud), $\mathbf{r_i}$ (θ_i) is the cell position (orientation), m_i ($I_i = \frac{1}{8}Ma^2\left(\frac{1+\Delta^4}{1+\Delta^2} + 2\left(\frac{(1+\Delta)\Delta}{1+\Delta^2}\right)^2\right)$ with $\Delta_i = \sigma_{i,\mathrm{bud}}/\sigma_{i,\mathrm{mother}}$) is the cell mass (inertia), V is the total potential energy, $\mathbf{F_i} = -\nabla_{\mathbf{r_i}}\mathbf{V}$ ($T_i = -\partial_{\theta_i} V$) is the force (torque) on cell i, and $\delta_{ik,jl} = \frac{1}{2}\left(\sigma_{ik} + \sigma_{jl}\right) - \left|\mathbf{r_{ik}} - \mathbf{r_{jl}}\right|$ is the overlap between lobes k of cell i and l of cell j, and Θ is the Heaviside Step function. This method is similar to studies performed with growing spherocylinders [11, 12]. For simulations with attraction, we extend the potential in Eq. 4 beyond its repulsive core to have an attractive range of width Δ [13, 14]

$$V = \sum_{ikjl}\left(\frac{1}{2}k_{\mathrm{CG}}\delta_{ik,jl}^2\Theta(\delta_{im,jn}+\Delta) - \frac{1}{2}k_{\mathrm{CG}}\Delta^2\right) \quad (10)$$

In this model, the mother lobe has the same size $\sigma_{i,\mathrm{mother}} = \sigma$ for all cells. Equations of motions are integrated using a 3rd order Gear Predictor-Corrector algorithm. Growth progresses while $\sigma_{i,\mathrm{bud}} < \sigma$ and culminates in division. After division, both new cells retain the orientation of cell i.

Cells grow in a rectangular box of dimensions $L_x \times L_y$ with an outlet of width a. For the simulations in this paper, we used $L_x = 6\sigma$, $L_y = 16\sigma$, and $a = 1.4\sigma$ to match experiments unless stated otherwise. Cells interact with the wall with the same cell-cell repulsive spring force, $V_{\mathrm{wall}} = \frac{1}{2}k_{\mathrm{CG}}\delta^2\Theta(\delta)$, where δ is the overlap between the cell and wall.

Without pressure feedback, $\gamma_i = \gamma_i^0$ where γ_i^0 is chosen from a uniform distribution of width 20% around a mean growth rate γ. With pressure feedback, the growth rate depends on pressure as $\gamma_i = \gamma_i^0 e^{-P_i/P_0}$ where P_i is the pressure of cell i.

The free parameters in this model are an effective friction coefficient $\mu/\left(\gamma\sqrt{mk_{\mathrm{CG}}}\right)$ and a characteristic pressure feedback scale P_0/k. In Fig. 3 of the main text, we use parameters that best matches the experimental pressure fluctuations in the case of intermittent flow where the pressure slowly builds and then suddenly drops during avalanches. We choose values of $\mu = 8\times10^4\gamma\sqrt{mk_{\mathrm{CG}}}$ and $\mu = 2\times10^3\gamma\sqrt{mk_{\mathrm{CG}}}$ for simulations with (Fig. 2b) and without (Fig. 2c) feedback that best capture the ratio of pressure increase ($\dot{P}_\uparrow$) and drop ($\dot{P}_\downarrow$) rates in the case as shown in Fig. S10. To obtain an experimentally-motivated value of feedback pressure P_0 (Fig. 2c), we used a value of P_0 that yields the same ratio of $P_0^{\mathrm{exp}} = 0.28$ MPa (Fig. 3c) to $\langle P\rangle^{\mathrm{exp}} = 0.7$ MPa (135° data in Fig. 1c), $P_0^{\mathrm{exp}}/\langle P\rangle^{\mathrm{exp}} = 0.4$. Coarse-grained simulations without feedback yield $\langle P\rangle^{\mathrm{sim}} = 0.19k_{\mathrm{CG}}$, giving $P_0^{\mathrm{sim}} = \langle P\rangle^{\mathrm{sim}} \times P_0^{\mathrm{exp}}/\langle P\rangle^{\mathrm{exp}} = 0.07k$.

Estimation of pressure due to viscous friction: Here we estimate the pressure arising from friction between cells in the outlet and the surrounding medium. In a chamber of dimensions $L_x \times L_y$ with an outlet of dimensions width×length$= a \times d$, the chamber holds $N_c \approx L_x L_y h/\sigma^3$ cells and the outlet holds $N_o \approx adh/\sigma^3$ cells, where σ is a typical cell diameter and h is the height of the device. Assuming that the height h of the system and the width of the outlet a are both $a = h = \sigma$, so that $N_c \approx L_x L_y/\sigma^2$ and $N_o \approx ad/\sigma^2$. If the cells in the outlet are pushed out at velocity v, the total frictional force they experience is $F = fvN_o$, where f is a friction coefficient per cell, and therefore the pressure at the outlet is

$$P = F/(ah) = fvN_o/\sigma^2 \tag{11}$$

Standard viscous friction of a sphere in a liquid yields $f = 6\pi\eta\sigma/2$. We further estimate the flow velocity by $v = N_c\sigma k$ where k is the growth rate for cells in the chamber, assuming that cells in the outlet are not growing. This gives:

$$P = \left(6\pi\eta\sigma/2\right)\left(N_c\sigma k\right)N_o/\sigma^2 \tag{12}$$
$$= 3\pi k\eta N_o N_c \tag{13}$$

Using $\eta = 10^{-3}$Pa s, $k \approx 0.4\text{h}^{-1} \approx 10^{-4}\text{s}^{-1}$, $N_c \approx 100$, and $N_o \approx 10$, we get

$$P = 3\pi k\eta N_o N_c \tag{14}$$
$$= 3\pi \times 10^{-3} Pas \times 10^{-4} s^{-1} \times 100 \times 10 \tag{15}$$
$$= 1 \times 10^{-3} Pa \tag{16}$$

Thus, viscous friction gives a negligible contribution to the pressure generated in the outlet, which is in the MPa range.
Conversely, we can use the above estimate to define an effective viscosity of the cell packing of 1 MPa s needed to achieve a pressure of 1 MPa. This effective viscosity is much larger than has been measured for mammalian cells [15].

Code and microfluidic design availability

All the codes used in this study, as well as all the microfluidic blueprints are available on request.

Supplementary Figures

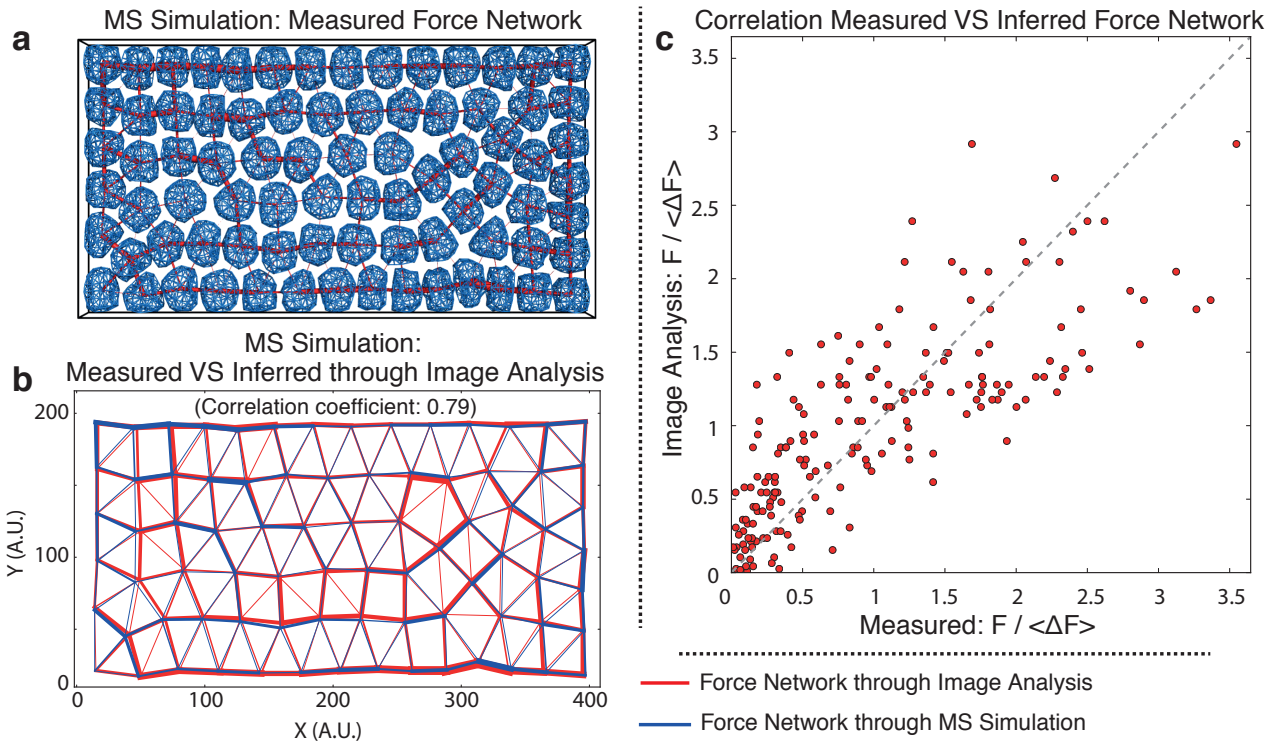

Figure S1: **Testing our indirect force-inference method on simulated packings**. In the main text, we reported mechanical forces in packings of yeast cells that we have inferred from the observed cell shape deformations. Our force-inference method uses use a custom Matlab image analysis code to process the time-lapse movies that we obtained with the fluorescence exclusion method (Fig. S2). Each cell is identified with a watershed algorithm and manually refined if necessary. For each identified cell, the contour is defined as a set of spline functions. These splines are further used to calculate the length l of the contact line between each pair of cells. As a first order approximation, we estimate the contact area as $A \propto l^2$, and we assume that the contact force is proportional to the contact area $F \propto A$ (Materials and Methods: See Inferring force maps). Here, we test our force-inference method on packing generated by our mass-spring simulation. To this end, we compare the inferred force network with the actual force network in the simulations. (**a**) 80 cells of the same size ($R_0 = 1.5\mu$m), turgor pressure ($\Pi = 1.0$ MPa), and E=100 MPa are randomly distributed and compressed in a slab geometry. The cells are depicted as a semi-transparent blue meshwork, confined by the rigid box. The contact forces are evaluated numerically and are represented as the red lines between neighbor cells. The thickness of the lines corresponds to the magnitude of the contact forces. (**b**) The final snapshot from the simulation is processed with the in-house Matlab code for image analysis, and contact forces have been inferred. The numerical (in blue) and image analysis (in red) force networks are superimposed on top of each other for visual comparison. The correlation coefficient calculated for these two sets of contact forces is 0.79. (**c**) Scatter plot of each contact force in **b**. Forces have been scaled by the average value. Measured are the forces obtained from the mass-spring simulations, and compared against the one obtained from the image analysis procedure.

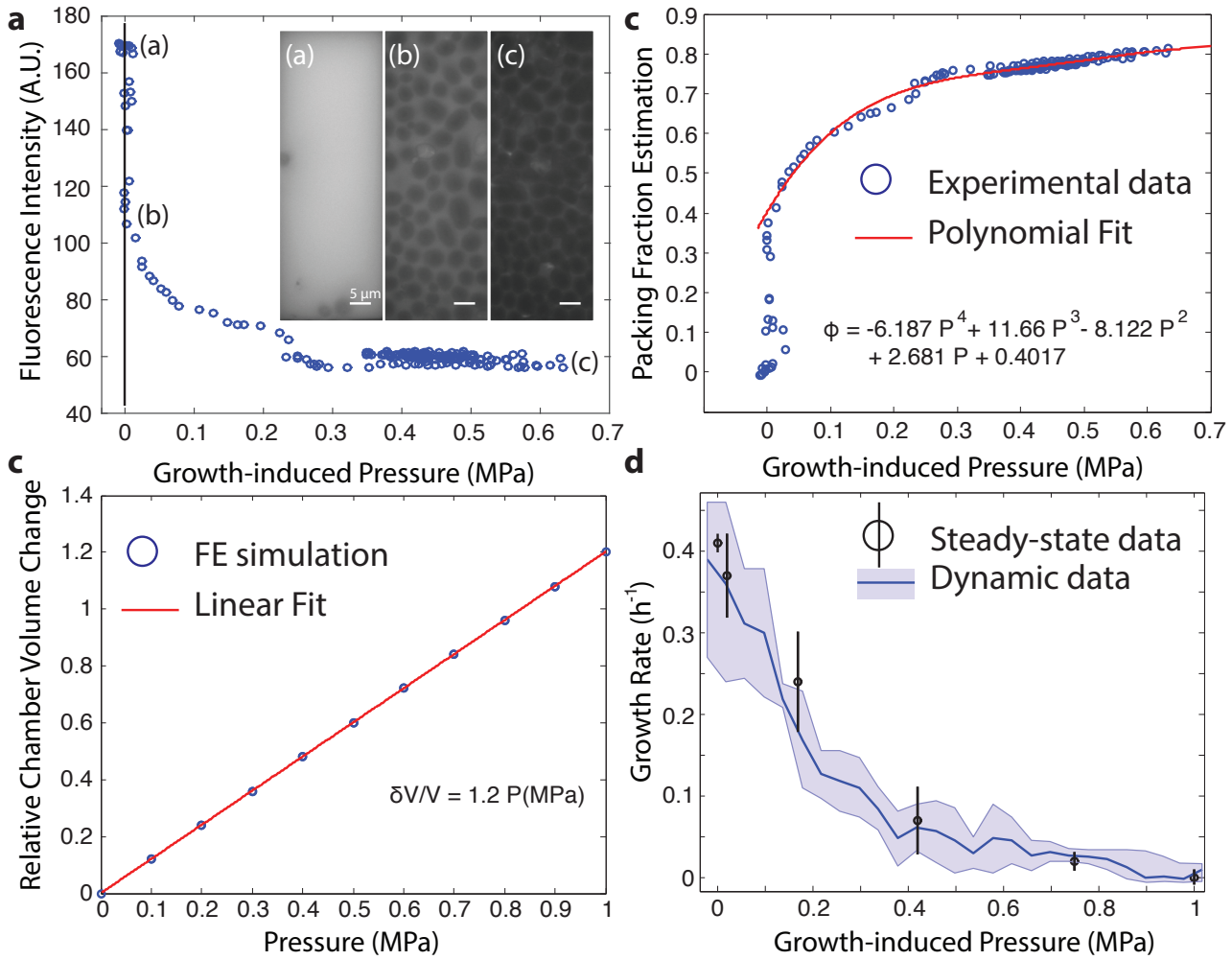

Figure S2: **Inferring the instantaneous growth rate as a function of pressure using the pressure curve obtained from the self-closing valve.** (**a**) A fluorescent dye, FITC-conjugated Dextran, added to the medium allows us to label the space between the cells. FITC-conjugated Dextran does not penetrate inside the cells, such that its fluorescence is excluded from a cell. As a consequence, as the cells are filling the chamber, the fluorescence intensity is, in first order, proportional to the void in between cells, like in the fluorescent exclusion method [16]. Denoting ϕ the packing fraction, and V the volume of the chamber, we assume that the intensity I of fluorophore is $I \propto (1-\phi)V$. (**b**) We use finite element simulations (Comsol) to estimate the change in volume of the growth chamber as a function of the pressure. We define the PDMS as a hyperelastic material as in [17], with an estimated Young's modulus E = 2MPa. We find that the change in volume is to good approximation linear in the pressure. (**c**) We use the excluded fluorescence, as well as the finite element simulation, to estimate the cell packing fraction, ϕ, as a function of the growth-induced pressure. We observe that the growth-induced pressure starts to rise in the chamber for a packing fraction of about 0.4. We fit the resulting relationship by a forth order polynomial function to obtain a continuously differentiable function. (**d**) We use the values extracted from b and c to calculate the instantaneous volumetric growth rate γ, using a quasi-steady state assumption as described in the Supplementary Method (see Measuring the steady-state and instantaneous growth rate). The dark blue line corresponds to the values calculated from the mean pressure, and the envelope corresponds to the values calculated from the envelope of the pressure curve. Note that the inferred continuous relationship between growth rate and contact pressure is in good agreement with the steady-state data obtained independently, from outflow rates in our leaky devices (black points, mean $\pm$ standard deviation).

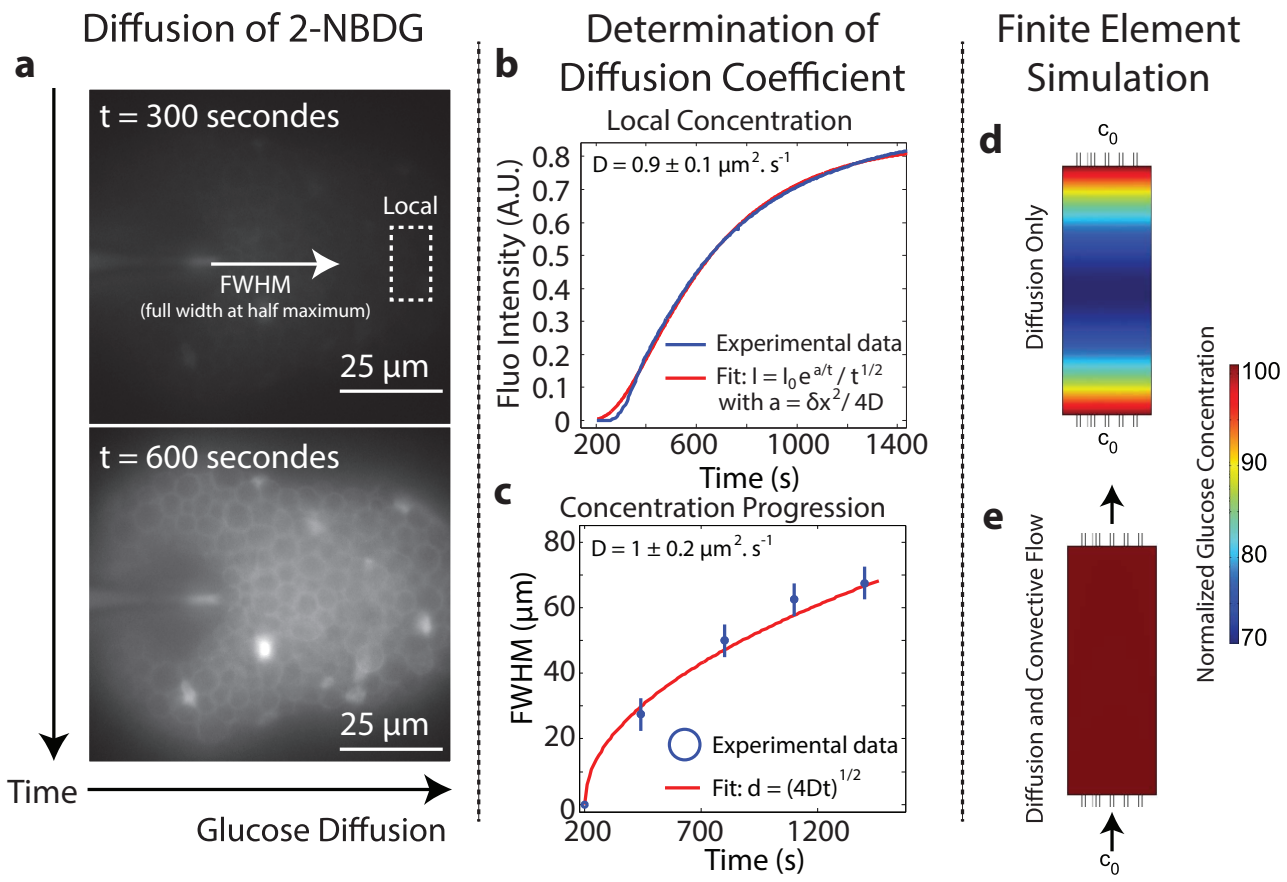

Figure S3: **The reduction of growth rate is not due to glucose depletion in the growth chamber**. To estimate whether glucose depletion could account for the observed reduction of growth rate, we assume that cells would locally consume glucose at the maximum rate. We consider two cases: either glucose merely diffuses inside the growth chamber, or it is also advected by the imposed nutrient flow. In both cases, we find that the reduction of glucose concentration in the chamber is not enough to stall cell growth. (**a**) We first measure the diffusion of 2-NDBG, a fluorescent glucose analog molecule. Here, we observe at the beginning of the experiment that there is almost no glucose in the self closing valve, and that it progressively diffuses in the chamber. Notice the foam-like packing of the cells, which results from the growth-induced pressure nearly balancing the turgor pressure. (**b - c**) We measure the diffusion constant of the glucose analog in 2 different ways. We measure either the local concentration at a fixed position in the chamber (**b**) or the full width at half maximum (FWHM) as a function of time (**c**, mean ± standard deviation). Fitting of a simple diffusion model agrees well with the experimental data, and enables us to extract values for the diffusion constant of the glucose analog (see figure). (**d - e**) The biomass yield of *S. cerevisiae* cells is $0.45 \times g_{cells}/g_{glucose}$ [18]. With a minimum doubling time of 2 hours, this yields a glucose consumption rate of 2.2×10^7 molecules/s. We simulate glucose consumption in the fully packed growth chamber using finite element simulations (Comsol) and the measured glucose diffusion constant extracted in **b** and **c**. We consider two cases: either there is only consumption and diffusion (**d**) or consumption, diffusion and convection (**e**). We find that in the case where there is only diffusion, the glucose concentration drops at about 70% of its boundary value c_0, which is about 14 g/L, and still above the concentration where depletion of glucose affects growth [19]. In a finite element simulation set-up where we impose a convective flow of 0.2 nL/s, we observe that there is no glucose gradient in the growth chamber. We conclude that the observed reduction of growth rate in figure 3c is not an effect of glucose depletion in the growth chamber.

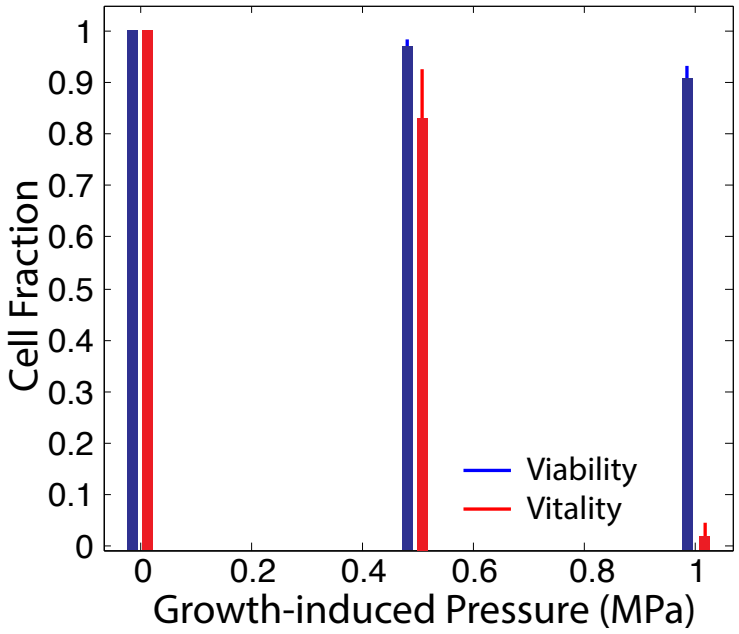

Figure S4: **Measurement of cell viability and cell vitality.** We assess how pressure changes cell viability and metabolic activity. Cell viability is assessed through a viability kit (LIVE/DEAD Yeast Viability Kit, Thermo Fisher Scientific). Briefly, propidium iodide (PI) is added to the culture medium. PI only enters the nucleus of dead cells and binds to DNA. We observe that, even at maximum pressure, most of the cells are alive (more than 90% of the cells). Cell vitality is assessed by adding a cell permeable esterase substrate (FungaLight Yeast CFDA, AM, Thermo Fisher Scientific) that is cleaved by esterases. The cleaved molecule becomes fluorescent, which enables one to assess esterase activity, which is directly linked to the global cell metabolic activity. We observe that, even though cell vitality does not change much at 0.5 MPa (the change is less than 15%), it is almost non existent at the maximum pressure of 1MPa. This suggests that, even though alive, cells are not metabolically active. This could be explained by pressure-induced molecular crowding, as in [20], where all processes in the cell are slowed down to the point of stalling by the very high compression. Note that at the highest pressure, we observe about 5% of the cells bursting. The data represent, for $N \geq 3$ independent replicates, the mean $\pm$ standard deviation.

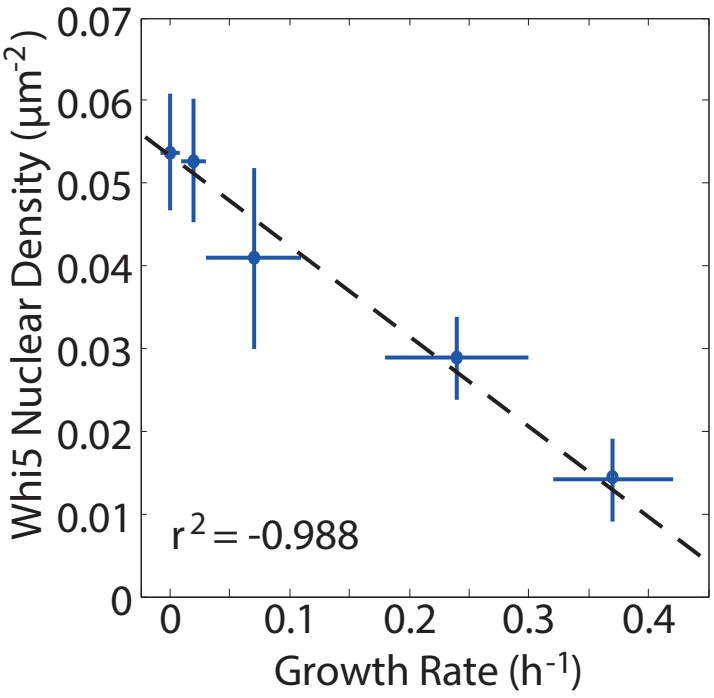

Figure S5: **The density of nuclear Whi5 is anti-correlated with the growth rate.** This plot shows the nuclear Whi5 density for different growth-induced pressures. The Whi5 density was obtained by measuring the number of cells with a nuclear Whi5 normalized by the observed area. Note that the nuclear density of Whi5 is increasing with decreasing growth rate, suggesting that growth rate reduction is accompanied with a cell cycle delay in the G1 phase of the cell cycle. Errors are mean $\pm$ standard deviation for $N \geq 5$ independent replicates.

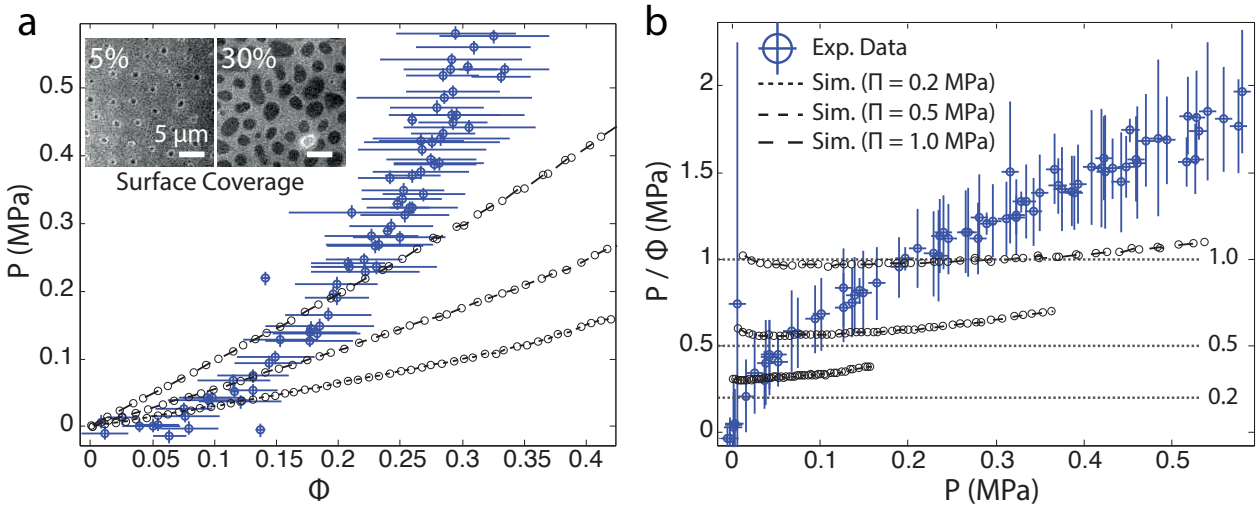

Figure S6: **Relationship between fraction of surface covered and growth-induced pressure indicates turgor pressure adaptation.** (**a**) The growth-induced pressure increases (circles) faster than linearly with the fraction of surface covered. Typical pictures obtained by reflectometry are presented in the inset for different values of surface coverage. The dashed lines are obtained from our mass-spring simulations, in which yeast cells are modeled as elastic shells subject to a *constant* turgor pressure. The simulations yield a growth-induced pressure that increases linearly with surface coverage. The slope is equal to the turgor pressure Π, for which we chose three different values. The discrepancy between data and simulations suggests that the turgor pressure increases with growth-induced pressure. (**b**) The growth-induced pressure divided by the fraction of covered surface corresponds to the pressure exerted in the contacts between cells and cover slip. Accordingly, the constant turgor pressure simulations of elastic shells yield nearly horizontal lines. The data, however, clearly shows that the pressure in the cell-coverslip contacts increase with the growth-induced pressure. This may indicate a gradual increase in turgor pressure. Error bars of the simulation data are smaller than the symbols. Error bars for the surface coverage are estimated as followed: We assume that we cannot measure the contact better than the diffraction limit. Hence, assuming a circular contact, we write that the radius of the contact has a typical error of $\pm\delta$, where δ is the radius of the Point Spread Function.

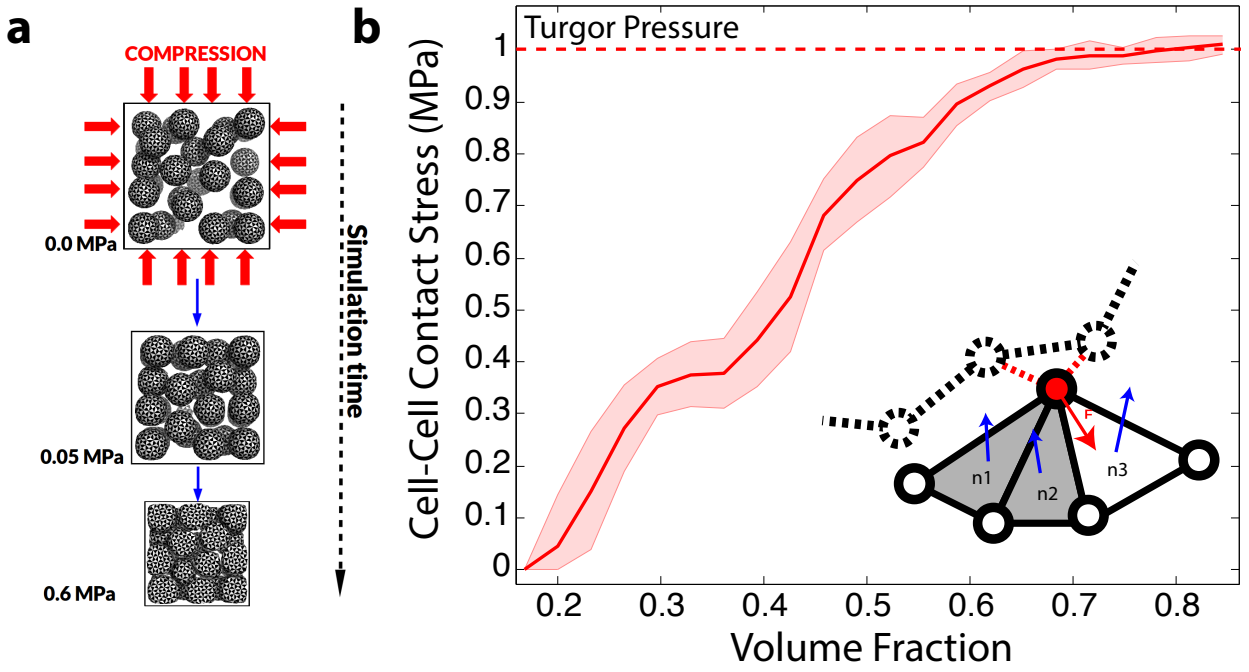

Figure S7: **The average cell-cell contact stress approaches the cell turgor pressure under high compressive stress.** We measure the cell-cell contact stress in mass-spring simulations, and find that for high compression / packing fraction, the stress approaches the internal cell turgor pressure. (**a**) Mass-spring simulations scheme. Identical cells are randomly distributed in a rigid box. The initial concentration is low so the cells do not touch one another. The simulation box is progressively compressed, hence increasing the packing fraction. (**b**) 50 identical cells ($R_0 = 2.5\mu$m, $\Pi = 1.0$ MPa, E = 150 MPa, t = 0.1μm) are compressed. For each pair of cells, the contact stress is calculated and the average contact stress is plotted (red line) versus the fraction of box volume occupied by cells. For high compression (>0.7) the value of the average contact stress saturates at the value equal to turgor pressure, 1 MPa. The envelope corresponds to $\pm$ standard deviation and is obtained out of 5 replicates simulations with different random initial cell positions and orientations. **Inset.** The contact stress is calculated as a ratio of the total normal force between two cells F_n and total contact area A_c. The contact area A_c on one cell is a sum of areas of all triangles being in contact with the other cell. A triangle is in contact with another cell if all its vertices are in contact with the neighbor cell (non-zero repulsive forces). The total normal force exerted on one cell is a sum of all normal forces exerted on each vertex by the neighbor cell. To calculate the normal force $\mathbf{F}$ (red arrow) acting on a vertex (black-red circle), first the sum of all non-bonded repulsive forces, $\mathbf{F}_{rep}$ (red dashed lines), is calculated. Next the normal component of this force is extracted as a dot product with all the triangles (described by the normal vectors $\mathbf{n}_i$) being in contact with the neighboring cell (shaded triangles), $\mathbf{n}_i \cdot \mathbf{F}_{rep}$. In order to avoid double counting of the normal component of the force $\mathbf{F}_{rep}$, each dot product with $\mathbf{n}_i$ (here i=1,2) is multiplied by the area of the triangle on which the force $\mathbf{F}_{rep}$ is acting, and divided by the total contact area (it is the sum of areas of shaded triangles $A = A_1 + A_2$).

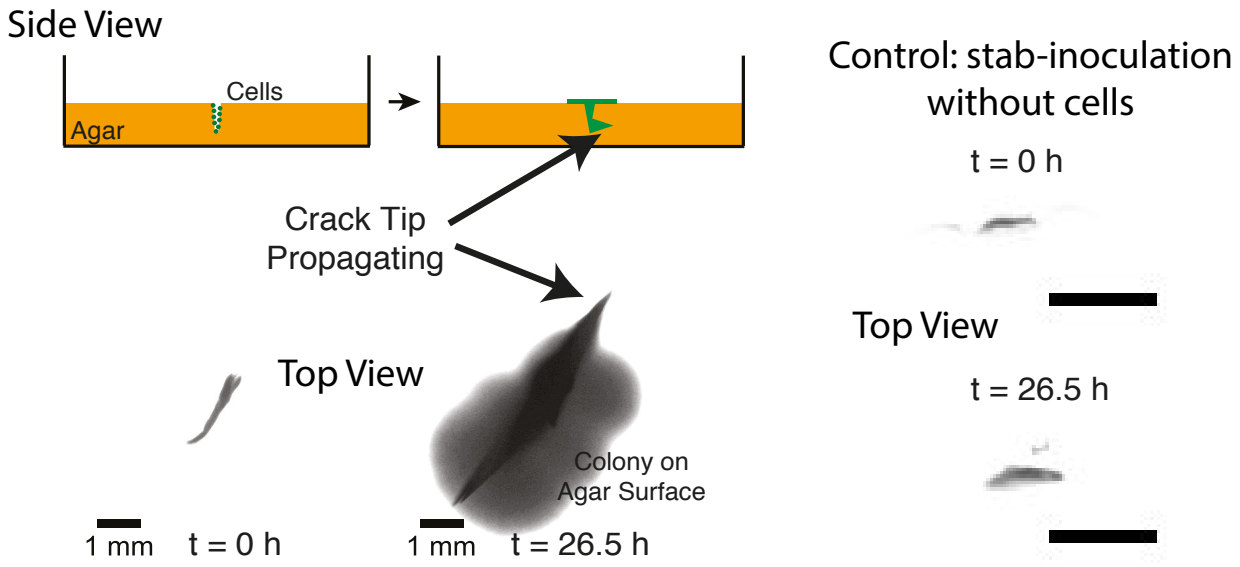

Figure S8: **Self-driven jamming can propagate cracks in agar gels.** We inoculate an agar gel (2%) by plunging in it a 0.45 mm diameter needle, which was first dipped in an overnight culture of budding yeast (strain S288C). The agar dish is then incubated at 30 degree Celsius under humidity control (to avoid drying). As the cartoon illustrates, cells flow out of the crack, and grow on the surface of the agar gel. The cells on top of the dish give rise to the large cloud on the lower image observed at 26.5 h, showing that the cells are not fully trapped in the crack. Nevertheless, the crack tips are propagating as a function of time, presumably due to jamming. As a control, we show images of cracks that were created by stabbing without cells and then incubated for the same amount of time. A time-lapse movie of the crack propagation is available `Movie S5`.

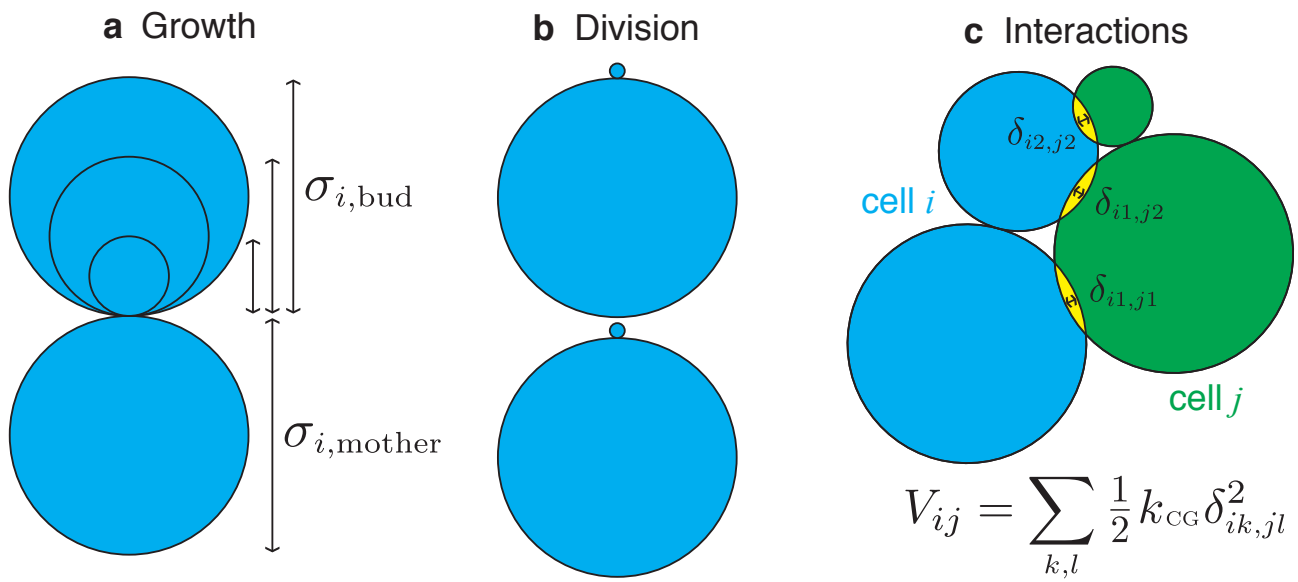

Figure S9: **How cells grow in our coarse-grain simulation.** Schematic of **a** the growth and **b** division processes and **c** inter-cell interactions in our coarse-grained simulations. Each cell is composed to two lobes, the mother and bud. **a** During growth, the mother lobe diameter of cell i stays fixed at $\sigma_{i,\mathrm{mother}} = \sigma$ while the bud grows from $\sigma_{i,\mathrm{bud}} = 0$ to $\sigma_{i,\mathrm{mother}} = \sigma$. **b** Once the bud reaches $\sigma_{i,\mathrm{mother}} = \sigma$, cell i divides into two new daughter cells that retain the orientation of their mother cell. **c** Cells i and j interact via only upon overlap via repulsive linear spring interactions with modulus k.

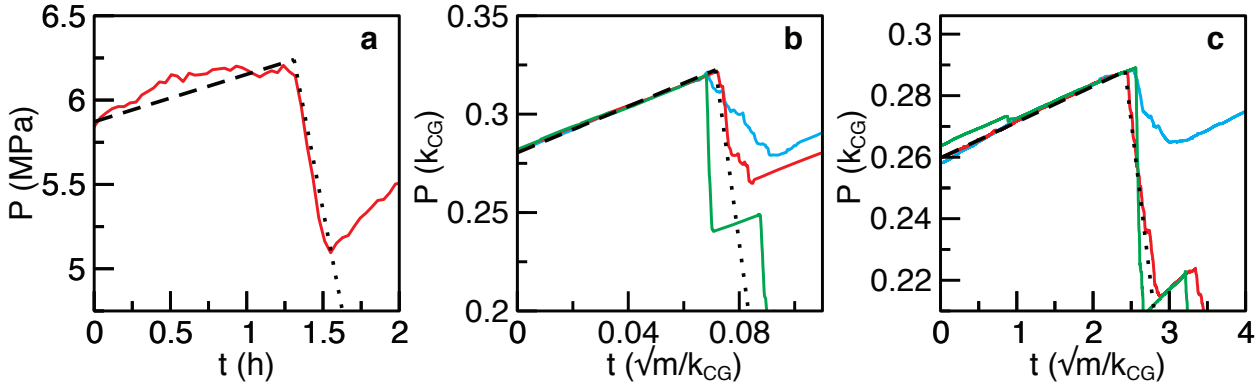

Figure S10: **How we parameterize our coarse-grain simulation.** We use the experimental pressure curves to parameterize our coarse-grain simulations: the pressure rise enables to parameterize the growth, and the pressure drop the damping rate. (**a**) Pressure as function of time during a single pressure drop for experiments. (**b**) Pressure as function of time during a single pressure drop for simulations without feedback. (**c**) Pressure as function of time during a single pressure drop for simulations with feedback ($P_0/k = 0.07$). The red line in **a** corresponds to experiments with an outlet gate with an angle of 135°. The red lines in **b** and **c** corresponds to simulations with best-fit values of μ (**b**: $\mu = 8 \times 10^4 \gamma\sqrt{mk_{\mathrm{CG}}}$ and **c**: $\mu = 2 \times 10^3 \gamma\sqrt{mk_{\mathrm{CG}}}$) used in Fig. 2b and Fig. 2c of the main text, the cyan line corresponds to larger values of μ (**b**: $\mu = 3.2 \times 10^5 \gamma\sqrt{mk_{\mathrm{CG}}}$ and **c**: $\mu = 8 \times 10^4 \gamma\sqrt{mk_{\mathrm{CG}}}$) and the green line corresponds to smaller values of μ (**b**: $\mu = 2 \times 10^4 \gamma\sqrt{mk_{\mathrm{CG}}}$ and **c**: $\mu = 5 \times 10^2 \gamma\sqrt{mk_{\mathrm{CG}}}$). For **a**, the dashed line shows the mean slope during pressure increase $\left(\dot{P}_{\uparrow}^{\mathrm{exp}}\right)$ and the dotted line shows mean slope during avalanche $\left(\dot{P}_{\downarrow}^{\mathrm{exp}}\right)$. For **b** and **c**, the dashed line is the mean slope during increase $\left(\dot{P}_{\uparrow}^{\mathrm{sim}}\right)$ and the dotted line shows the extracted value of $\dot{P}_{\downarrow}^{\mathrm{sim}}$ that yields the same ratio of $\dot{P}_{\downarrow}/\dot{P}_{\uparrow}$ as experiments.

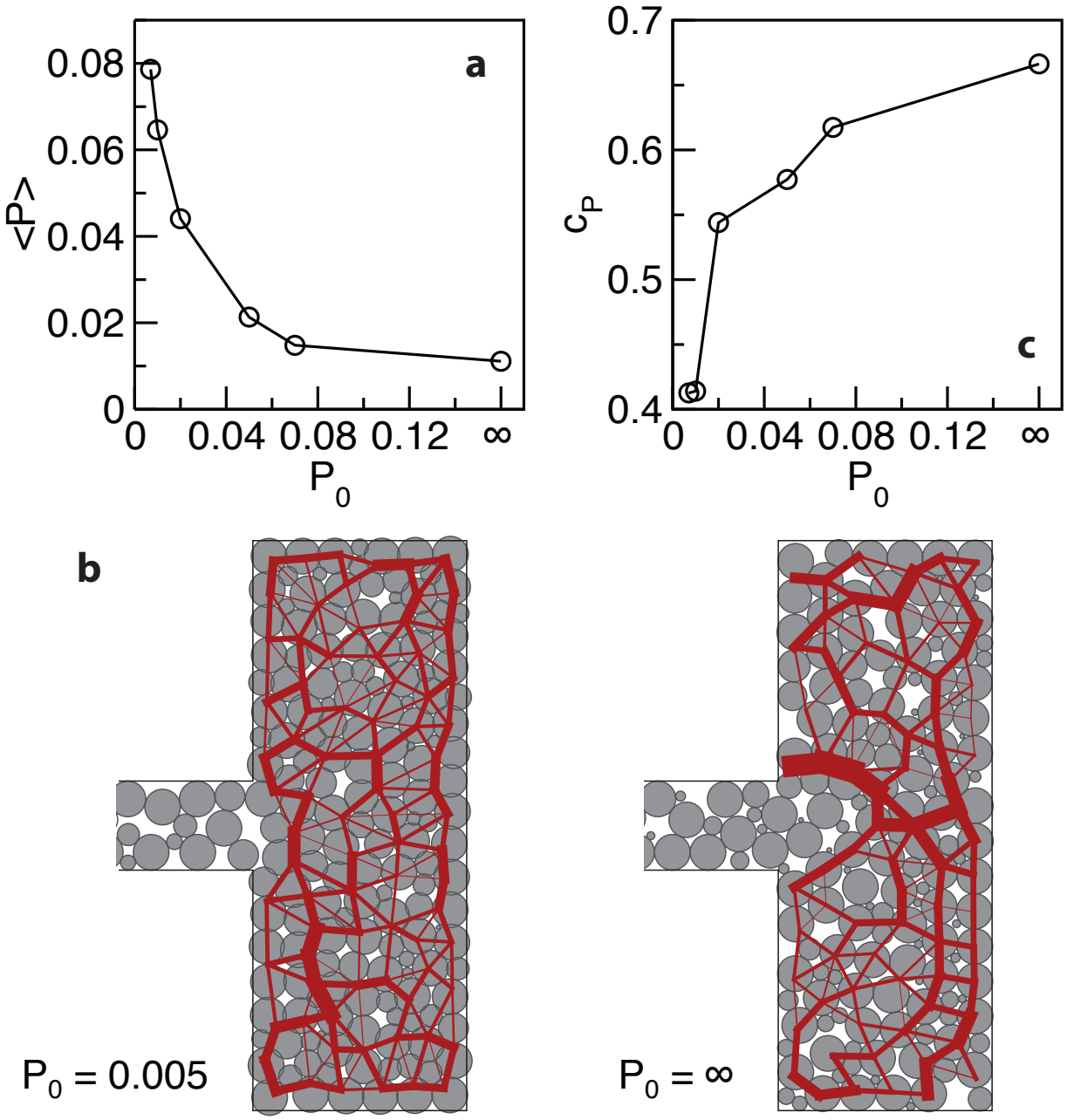

Figure S11: **Effect of feedback on force networks in coarse-grained simulations.** (**a**) In simulations where individual cell growth rates (k_i) decrease exponentially with pressure (P_i), $k_i \propto e^{-P_i/P_0}$, we observe that the time-averaged steady-state population pressure $\langle P \rangle$ increases as the feedback becomes stronger (P_0 decreases). $\langle P \rangle$ increases with decreasing P_0 because cell growth slows for $\langle P \rangle > P_0$, causing the population to spend more time at larger pressures. (**b**) Furthermore, feedback homogenizes force networks as illustrated by representative configurations without feedback and a heterogeneous force network ($P_0 = \infty$) and with strong feedback and a homogeneous force network ($P_0 = 0.005$). The reason for this homogenization is that low-pressure cells grow more quickly than high-pressure cells and fill in gaps in the force network. (**c**). We see that force-network homogenization is a strong effect - the coefficient of variation of individual cell pressures $c_P = \sqrt{\langle P^2 \rangle / \langle P \rangle^2 - 1}$ decreases by 40% with decreasing P_0

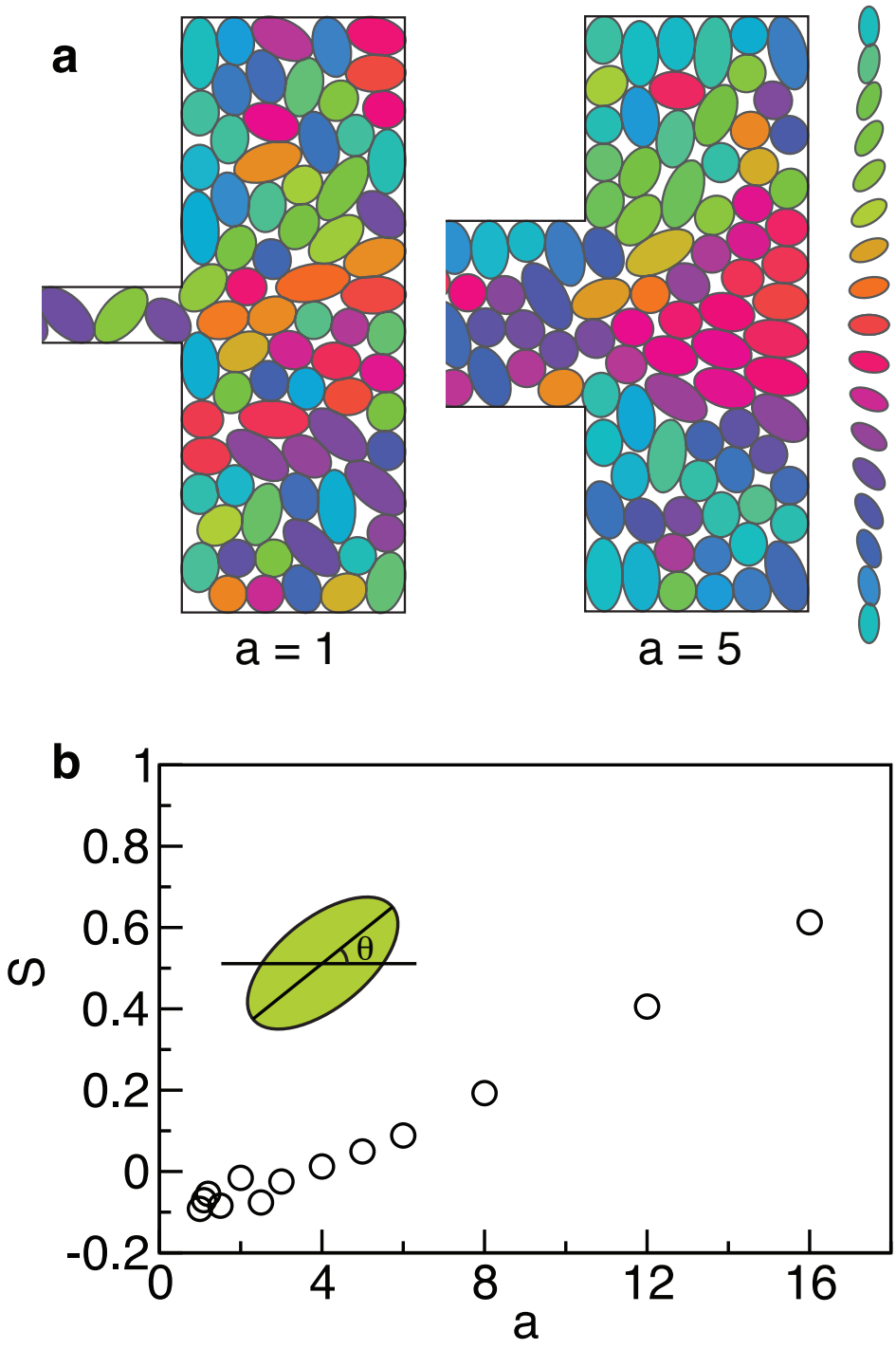

Figure S12: **Orientational alignment in coarse-grained simulations of elongated cells.** Simulations of proliferating ellipsoidal cells show that cells orientationally align in the direction of the outlet. (**a**) This alignment is stronger for wider outlet channels, illustrated for outlets channel widths of $a = 1$ which has very little alignment and $a = 5\sigma$ which has significant alignment. (**b**) We can quantify the degree of alignment via a nematic order parameter $S = \langle cos(2\theta) \rangle$, which measures the mean alignment of cells with the horizontal axis. S shows that orientations are disordered for $a < 4$ and become increasingly aligned with the horizontal axis as a increases.

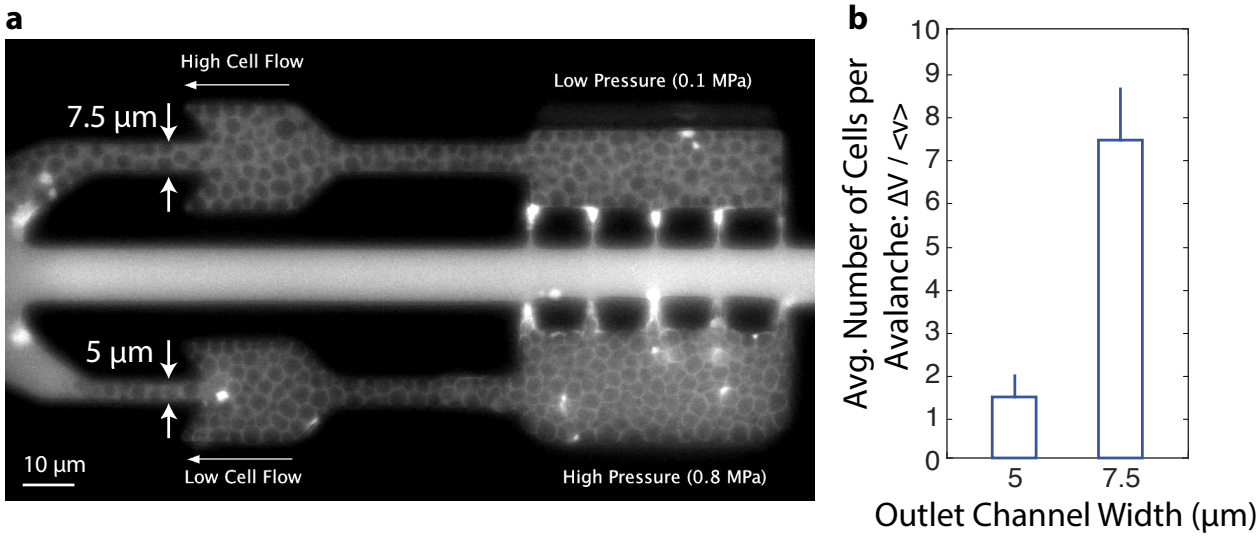

Figure S13: **Effect of outlet channel width on mean avalanche size.** We analyzed the movie (**Movie S2**), which was also referenced in the main text for a direct comparison of growth under different contact pressures. (**a**) Snapshot of the time-lapse movie, showing the two filled growth chambers connected in the same way to a single nutrient channel. The outlets of both chambers are connected to an outlet gate with an angle of 135^o, but the outlets have a different channel width, of 5μm and 7.5μm. We observe in this movie that the cells coming out of the outlet with a channel width of 7.5μm develop less pressure than the cells in the 5μm outlet channel width, and exhibit more avalanche events. (**b**) We measure for each avalanche, defined as the duration from when cells start to move until the next moment of stasis, the displacement l of the cell population in the channel. We then calculate the mean cell volume displacement, $\Delta V = l \times A$, where A is the cross-section of the outlet channel. An estimate of the average number of cells per avalanche is then obtained by dividing ΔV by a typical cell volume of $< v >$ = 65.5 fL. This volume corresponds to a mean cell diameter of 5μm. We note that the average size of an avalanche increases with increased outlet channel width (mean $\pm$ standard deviation for $N \geq 10$ avalanches).

References

[1] Anderson, J.R., Chiu, D.T., Wu, H., Schueller, O.J. and Whitesides, G.M. Fabrication of microfluidic systems in poly(dimethylsiloxane). *Electrophoresis* **21**, 27–40 (2000).

[2] Wu, Z. and Hjort K. Surface modification of PDMS by gradient-induced micrgraion of embedded pluronic. *Lab on a Chip* **9**, 1500–1503 (2009).

[3] Preston R.A., Murphy, R.F. and Jones, E.W. Apparent endocytosis of fluorescein isothiocyante-conjugated dextran by *Saccharomyces cerevisiae* reflects uptake of low molecular weight impurities, dextran. *The journal of cell biology* **105**, 1981–1987 (1987).

[4] Martinez de Maranon, I., Maréchal, P.A. and Gervais, P. Passive response of *Saccharomyces cerevisiae* to osmotic shift: cell volume variations depending on the physiological state. *Biochemical and biophysical research communications* **227**, 519–523 (1996).

[5] Stenson, J.D., Thomas, C.R. and Hartley, P. Modelling the mechanical properties of yeast cells. *Chemical Engineering Science* **64**, 1892–1903 (2009).

[6] Stenson, J.D., Hartley, P., Wang, C. and Thomas, C.R. Determining the mechanical properties of yeast cell walls. *Biotechnology progress* **27**, 505–512 (2011).

[7] Feng, W.W. and Yang, W.H. On the contact problem of an inflated spherical nonlinear membrane. *Journal of Applied Mechanics* **40**, 209–214 (1973).

[8] Smith, A.E., Zhang, Z., Thoma, C.R., Moxham, K.E. and Middelberg, A.P.J. The mechanical properties of *Saccharomyces cerevisiae*. *Proceedings of the National Academy of Sciences* **97**, 9871–9874 (2000).

[9] Kot, M., Nagahashi, H. and Szymczak, P. Elastic moduli of simple mass spring models. *The visual computer* **31**, 1339–1350 (2015).

[10] Schreck, C.F., Xu, N and O'Hern, C.S. A comparison of jamming behavior in systemps composed of dimer and ellipse-shaped particles. *Soft Matter* **6**, 2960–2969 (2010).

[11] Farell, F.D.C, Hallatschek, O., Marenduzzo, D. and Waclaw, B. Mechanically driven growth of quasi-two-dimensional microbial colonies. *Physical Review Letter* **111**, 168101 (2013).

[12] Volfson; D., Cookson, S., Hasty, H. and Tsimring, L.S. Biomechanical ordering of dense cell populations. *Proceedings of the National Academy of Sciences* **105**, 15346–15351 (2008).

[13] Irani, E., Chaudhuri, P and Heussinger, C. Impact of attractive interactions on the rheology of dense athermal particles. *Physical Review Letter* **112**, 188303 (2014).

[14] Lois, G., Blawzdziewicz, J. and O'Hern, C.S. Jamming transition and new percolation universality classes in particulate systems with attraction. *Physical Review Letter* **100**, 028001 (2008).

[15] Guevorkian, K., Colbert, M.J., Durth, M., Dufour, S. and Brochard-Wyart, F. Aspiration of biological viscoelastic drops. *Physical Review Letter* **104**, 218101 (2010).

[16] Bottier, C. *et al*. Dynamic measurement of the height and volume of migrating cells by novel fluorescence microscopy technique. *Lab on a Chip* **11**, 3855–3863 (2011).

[17] Hardy, B.S., Uechi, K., Zhen, J. and Pirouz-Kavehpour, H. The deformation of flexible PDMS microchannels under a pressure induced flow. *Lab on a Chip* **9**, 935–938 (2009).

[18] Ertugay, N., Hamaci, H and Bayindirli, A. Fed-batch cultivation of bakers yeast: effect of nutrient depletion and heat stress on cell composition. *Folia microbiologica* **42**, 214–218 (1997).

[19] Youk, H. and van Oudenaarden, A. Growth landscape formed by perception and import of glucose in yeast. *Nature* **462**, 875–879 (2009).

[20] Hersen, P., McClean, M.N., Mahadevan, L. and Ramanathan, S. Signal processing by the hog MAP Kinase pathway. *Proceedings of the National Academy of Sciences* **105**, 7165–7170 (2008).